

## To editor

### Comments:

I have to say that I share a major concern on an issue identified by two of the reviewers about the implementation of the competition between heterogeneous and homogeneous ice nucleation in the cirrus regime. This is described in part 1, but is also crucial for the results in part 2. If the background aerosol concentration for homogeneous freezing of deliquesced aerosols is set to an unrealistically low value of  $1/L$ , all effects by adding dust are drastically exaggerated or can have the wrong sign. Furthermore, I still miss details on whether and how deposition ice nucleation (parameterized by Phillips et al 2008) is coupled to the dust concentration.

### Response:

1. We agree that the exclusion of water-friendly aerosols for this process in the simulations is unreasonable and might cause an exaggeration of the effect of dust on the cloud IWP. To address this concern, we have the simulations with actual number concentration of water-friendly aerosols instead of using a background aerosol number concentration of  $1/L$  for Koop's parameterization scheme. In revised manuscript, water-friendly aerosols were included in both CTRL and DUST simulations. The number concentration of water-friendly aerosols was read from the pre-given climatological aerosol profile derived from long-term simulations of global climate models. The aerosol profile was provided by Dr. Thompson and Dr. Eidhammer and used in their paper for evaluating the performance of the Thompson-Eidhammer microphysics scheme (Thompson and Eidhammer, 2014).

The results in the revised manuscript as well as Figures 6-12 have been updated, but our conclusions remain the same according to the simulation results. We have clarified the new configuration in Section 4 (Line 262-267).

2. The Phillips' parameterization scheme was included in the original Thompson-Eidhammer microphysics scheme and coupled with dust concentration, we did not make any modification on this scheme, and therefore we did not elaborate it in our manuscript. When the relative humidity with respect to ice ( $RH_i$ ) is above 105% and relative humidity with respect to water ( $RH_w$ ) is above 98.5%, it is counted as condensation and immersion freezing, and calculated by DeMott2015 scheme; When  $RH_i$  is above 105% and  $RH_w$  is below 98.5%, it is treated as deposition nucleation, and determined by the Phillips' parameterization scheme (Phillips et al., 2008). We have clarified it in Subsection 2.2 (line 130-135).

### To the anonymous referee

We deeply thank the anonymous referee again for the suggestions and comments. All the concerns of the reviewer have been addressed and the responses to each comment are listed below.

#### General comment:

I would ask again the authors to explain more clearly how the heterogeneous nucleation occur in the CTRL simulation where no aerosol emissions are considered. In the manuscript, the authors write that "...the freezing of deliquesced aerosols using the hygroscopic aerosol concentration is parameterized following Koop et al. 2000, with the background aerosol concentration set to be 1/L." at lines 256-257. However, they should explain this concept better in Section 4 so, please, review the lines 253-258. For example, it would be clearer if they could explain similarly to their answer to the Editor's comment, i.e.: "By the default setting in the aerosol-aware Thompson microphysics scheme, heterogeneous nucleation is still activated in the control simulation, but with a constant ice nuclei concentration of 1 per Liter."

Response: As the Editor and a referee for Part II of this paper pointed out that the freezing of the deliquesced aerosols has a great contribution to cloud IWP, however, we did not include water-friendly aerosols for this process in our simulations, which is unreasonable and might cause an exaggeration of the effect of dust on the cloud IWP. To address this concern, we have the simulations with actual number concentration of water-friendly aerosols instead of using a background aerosol number concentration of 1/L for Koop's parameterization scheme. In revised manuscript, water-friendly aerosols were included in both CTRL and DUST simulations. The number concentration of water-friendly aerosols was read from the pre-given climatological aerosol profile derived from long-term simulations of global climate models. The aerosol profile was provided by Dr. Thompson and Dr. Eidhammer and used in their paper for evaluating the performance of the Thompson-Eidhammer microphysics scheme (Thompson and Eidhammer, 2014).

The results in the revised manuscript as well as Figures 6-12 have been updated, but our conclusions remain the same according to the simulation results. We have clarified the new configuration in Section 4 (Line 262-267).

#### Minor comments:

Line 66: "is the most abundant aerosols": aerosols → aerosol.

Response: Corrected.

Lines 70-83: Thanks for the additional information about WRF and WRF-Chem. I personally find the order of the information not super clear, I mean: the authors say that the aerosol-aware Thompson-Eidhammer

microphysics scheme has been implemented in WRF, however, in lines 74-75 they make a contrast mentioning WRF-Chem, which is not introduced yet. It would be sufficient to write before (e.g. at line 72, after the citation) that the aerosol-aware Thompson-Eidhammer microphysics scheme has been implemented ALSO in "WRF-Chem, the Weather Research and Forecast model coupled with Chemistry".

Response: Revised as suggested.

Line 79: "or couple" → "or by coupling".

Response: Corrected.

Lines 90-94: The paragraph has to be corrected according to the new structure of the manuscript (there is a new Section now).

Response: Corrected.

Line 110: Why is "model" moved from line 111 (after "GOCART aerosol") to line 110 (after "scheme")? I would leave "GOCART aerosol model".

Response: Corrected.

Line 134: "ice crystal" should be changed with "INP".

Response: Revised.

Lines 154-156: In my opinion, the sentence "...WE APPLY the DeMott2015 ice nucleation scheme in the GOCART-Thompson microphysics scheme TO BE IMPLEMENTED, instead of the DeMott2010 scheme, in the default aerosol-aware Thompson-Eidhammer microphysics scheme to simulate the ice nucleation involving dust." is not as clear as the explanation the authors wrote in their answers: "Although the DeMott2015 scheme has been implemented in the code of the Thompson-Eidhammer scheme, it cannot be used without modifying the code. We modified the code to call the DeMott2015 scheme in Thompson-Eidhammer scheme for the condensation and immersion freezing in our simulations."

Response: Revised as suggested.

Line 161: Please, adjust the sentence "...it is treated as deposition nucleation, and determined by the parameterization of Phillips et al. (Phillips et al., 2008) is applied to account for deposition nucleation.". It could be: "...it is treated as deposition nucleation, and determined by the parameterization of Phillips et al. (2008)" or "...it is treated as deposition nucleation, and the parameterization of Phillips et al. (2008) is applied to account for deposition nucleation.".

Check how the citation Phillips et al. (Phillips et al., 2008) is written.

Response: Revised.

Line 163: Check how the citation "Koop et al. (Koop et al., 2000)" is written.

Response: Corrected.

Line 164: I would have kept "WRF-Chem", instead of "WRF", as WRF-Chem is the model used for the simulations.

Response: Revised.

Lines 233-236: The word "conducted" is repeated 4 times... it does not sound very nice.

Response: We have rewritten the sentence.

Line 254: The sentence "The newly-implemented GOCART-Thompson microphysics scheme." lacks a verb. Maybe it has been forgotten.

Response: Revised.

Lines 255-257: Check how the citations "Phillips et al. (Phillips et al., 2008)" and "Koop et al. (Koop et al., 2000)" are written.

Response: Corrected.

Line 328: "The number concentrationS of dust particles over East Asia were vertically integrated..."

Response: Corrected.

Lines 325-327: In the sentence "The dust particles in the fourth and fifth bins with effective diameters ranging from 6 to 20  $\mu\text{m}$  account for around 60% of the total mass of dust aerosols, and dust particles with diameters smaller than 6  $\mu\text{m}$  account for around 40% of the total mass of dust aerosols.", it is obvious that the second percentage is 40%. The authors could simply write: "The dust particles in the fourth and fifth bins with effective diameters ranging from 6 to 20  $\mu\text{m}$  account for the major part (around 60%) of the total mass of dust aerosols."

Response: Revised as suggested.

Line 340: "...the simulated PM10 concentrationS were extracted..."

Response: Corrected.

Line 342: The sentence "...thus here were five groups in Figure 3." does not sound completely correct.

Response: We have rewritten the sentence.

Line 344, 348: "PM10" → PM10".

Response: Corrected.

Line 345: Just as reminder to the reader: "...as no other emissions were considered in the simulations APART FROM DUST.".

Response: Revised as suggested.

Line 346: I am sorry, I do not see overestimations in Fig. 3e, rather in Fig. 3g and 3h.

Response: It was a mistake, we have revised it.

Line 375: Please, add the reference to Fig. 5 already here: "...from MODIS and MISR products IN FIGURE 5.", otherwise, the high values of AOD are described before any reference to the figure.

Response: Revised as suggested.

Lines 382-383: It is not clear if "respectively" refers to March and April. Please, check the sentence.

Response: We have added "March and April" before "respectively".

Lines 482-485: There is a repetition. Please, delete "by considering the effects of dust on ice nucleation process," or "by taking in to account the effect of dust in the ice nucleation process".

Response: Revised.

Line 519: "ro" → "to".

Response: Corrected.

Lines 540-551: Better "relative humidity threshold" instead of "threshold relative humidity". Also at lines 579 and 580. Also in the abstract at line 30.

Line 540: Here, which is the beginning of a new subsection, I would repeat "with respect to ice" (i.e. "...relative humidity threshold with respect to ice to trigger...").

Response: We have replace threshold relative humidity with respect to ice with RH, in the updated manuscript.

Lines 569-572: I think that this paragraph refers to the old Fig. 8, which has been removed.

Response: Revised.

Line 579: "3 or 4" is not consistent with "4 or 5" at line 529 (in my opinion the second option is better).

Response: Revised.

1 **Investigating the role of dust in ice nucleation within clouds and**  
2 **further effects on the regional weather system over East Asia**

3 **Part I: model development and validation**

4 Lin Su<sup>1</sup>, and Jimmy C.H. Fung<sup>2,3</sup>

5 <sup>1</sup>School of Science, Hong Kong University of Science and Technology, Hong Kong, China

6 <sup>2</sup>Division of Environment, Hong Kong University of Science and Technology, Hong Kong, China

7 <sup>3</sup>Department of Mathematics, Hong Kong University of Science and Technology, Hong Kong, China

8 *Correspondence to: Lin Su ([lsu@connect.ust.hk](mailto:lsu@connect.ust.hk))*

9

10 **Keywords:** dust; ice nucleation; microphysics scheme implementation; numerical modeling

11

12 **Highlights:**

13 A new treatment has been implemented in a regional model for evaluating the role of dust particles in atmospheric  
14 ice nucleation.

15 The effect of dust on atmospheric IWC over East Asia during a dust-intensive period is simulated.

16 The simulation of atmospheric IWC during dust events is substantially improved upon the effect of dust being  
17 considered.

18

19 **Abstract.** The GOCART–Thompson microphysics scheme coupling the GOCART aerosol model and the aerosol-  
20 aware Thompson-Eidhammer microphysics scheme has been implemented in ~~WRF-Chem~~the WRF-Chem, to quantify  
21 and evaluate the effect of dust on the ice nucleation process in the atmosphere by serving as ice nuclei ~~(IN)~~. The  
22 performance of the GOCART-Thompson microphysics scheme in simulating the effect of dust in atmospheric ice  
23 nucleation is then evaluated over East Asia during spring, a typical dust-intensive season, in 2012. Based upon the  
24 dust emission reasonably reproduced by WRF-Chem, the effect of dust on atmospheric cloud ice water content ~~(IWC)~~  
25 is well reproduced. With abundant dust particles serving as IN, the simulated ice water mixing ratio and ice crystal  
26 number concentration increases ~~by up to one order of magnitude~~15% and 7% in average over the dust source region  
27 and downwind areas during the investigated period. The comparison with ice water path from satellite observations  
28 demonstrated that the simulation of cloud ice profile is substantially improved by considering the indirect effect of  
29 dust particles in the simulations. Additional sensitivity experiments are carried out to optimize the parameters in the  
30 ice nucleation parameterization in the GOCART–Thompson microphysics scheme. Results suggest that lowering the  
31 threshold relative humidity with respect to ice -to 100% for the ice nucleation parameterization leads to further  
32 improvement in cloud ice simulation.

33

34



35 **1 Introduction**

36 Dust aerosol is the second largest contributor to the global aerosol burden (Textor et al., 2006), and it is estimated to  
37 contribute around 20% to the annual global aerosol emission (Tomasi et al., 2017). The Intergovernmental Panel on  
38 Climate Change (IPCC) has recognized dust as a major component of atmospheric aerosols, which are an “essential  
39 climate variable.” East Asia is a main contributor to the Earth’s dust emission. It has been reported in previous studies  
40 that East Asian dust contributes 25–50% of global emission, depending on the climate of the particular year (Ginoux  
41 et al., 2001).

42 Dust in the atmosphere alters the Earth’s weather and climate through certain ways. By reflecting, absorbing and  
43 scattering the incoming solar radiation, dust can cause a warming effect within the atmosphere and a cooling effect at  
44 the surface layer (Lacis, 1995), which is the direct effect of dust. The semi-direct effect of dust is related to the  
45 absorption of short-wave and long-wave radiation by dust aerosol within clouds, leading to a warming of the  
46 surrounding environment, causing a shrinking of cloud and a lower cloud albedo, and thus modifying the radiation  
47 budget (Perlwitz and Miller, 2010; Hansen et al., 1997). The dust-cloud-interaction is also referred to as the indirect  
48 effect of dust. Dust particles are recognized as effective IN and play an important role in the ice nucleation process in  
49 the atmosphere, directly affecting the dynamics in ice and mixed-phase clouds, such as the formation and development  
50 of clouds and precipitation (Koehler et al., 2010; Twohy et al., 2009).

51 To date, many studies have been conducted to evaluate the direct radiative effect of dust aerosol using radiation  
52 schemes implemented in numerical models all over the world (Mallet et al., 2009; Nabat et al., 2015a; Ge et al.,  
53 2010; Hartmann et al., 2013; Huang et al., 2009; Bi et al., 2013; Liu et al., 2011a; Liu et al., 2011b; Huang, 2017).  
54 Recently, semi-direct effect of dust has been investigated in a few studies over different regions by applying various  
55 global and regional models (Tesfaye et al., 2015; Nabat et al., 2015b; Seigel et al., 2013). Unfortunately, due to the  
56 poor understanding on the dust-cloud-interactions in microphysics processes, quantifying the microphysical effect of  
57 dust remains as a difficult problem. Various ice nucleation parameterizations have been implemented into global  
58 models to estimate the importance of dust in atmospheric ice nucleation (Lohmann and Diehl, 2006; Karydis et al.,  
59 2011; Hoose et al., 2008; Zhang et al., 2014). However, most regional models are not capable of estimating the indirect  
60 effect of dust, and very rare work has been done to assess the indirect effects of dust on the weather system, especially  
61 over East Asia, which is a major contributor to the global dust emission. Currently, only a few microphysics schemes

62 considering aerosol-cloud-interaction are implemented in regional models. In most of these microphysics schemes  
63 only the cloud condensation nuclei (CCN) served by aerosols are considered (Perlwitz and Miller, 2010;Solomos et  
64 al., 2011;Miller et al., 2004), while IN are not treated or represented by a prescribed IN distribution (Chapman et al.,  
65 2009;Baró et al., 2015), and the production of ice crystals is simplified by a function of temperature or ice saturation.  
66 In reality, however, the number of ice crystals that can form in the atmosphere is highly dependent on the number of  
67 particles that can act as IN, and dust is the most abundant aerosols that can effectively serve as IN and affect the  
68 formation and development of mixed-phase and ice clouds in the atmosphere. This effect should not be neglected in  
69 numerical models, especially in the simulations over arid regions during strong wind events (DeMott et al.,  
70 2003;Koehler et al., 2010;DeMott et al., 2015;Lohmann and Diehl, 2006;Atkinson et al., 2013).

71 In 2014, the aerosol-aware Thompson-Eidhammer microphysics scheme, which takes into account the aerosols  
72 serving as CCN and IN, has been implemented into the Weather Research and Forecast (WRF) model and also the  
73 Weather Research and Forecast model coupled with Chemistry (WRF-Chem), enabling the model to explicitly predict  
74 the number concentration for cloud droplets and ice crystals (Thompson and Eidhammer, 2014). Therefore, the  
75 aerosol-aware Thompson-Eidhammer scheme is an ideal microphysics scheme for evaluating the effect of dust in  
76 atmospheric ice nucleation processes. However, this scheme is not coupled with any aerosol model in WRF-Chem,  
77 the Weather Research and Forecast model coupled with Chemistry. When the aerosol-aware Thompson-Eidhammer  
78 microphysics scheme is activated, the model reads in pre-given climatological aerosol data derived from the output of  
79 other global climate models, which introduces large errors into the estimation of the effects of dust in microphysical  
80 processes. This problem can be solved by embedding a dust scheme into Thompson-Eidhammer scheme, or by  
81 couplingeouple the microphysics scheme with WRF-Chem. Compared with WRF, WRF-Chem integrates various  
82 emission schemes and aerosol mechanisms for simulating the emission, transport, mixing, and chemical  
83 transformation of aerosols simultaneously with the meteorology (Grell et al., 2013). Therefore, WRF-Chem is more  
84 capable of producing a realistic aerosol field by comparing the performances of different emission schemes or aerosol  
85 mechanisms.

86 In light of above, we aim to fully couple the aerosol-aware Thompson-Eidhammer microphysics scheme with the  
87 Goddard Chemistry Aerosol Radiation and Transport (GOCART) model (Ginoux et al., 2001) in the WRF-Chem  
88 modeling system in this study, enabling WRF-Chem to simultaneously simulate the effect of dust aerosol in ice

89 nucleation processes during simulations. Based upon the implementation, the performance of the coupled GOCART-  
90 Thompson microphysics scheme in simulating the ice nucleation process involving dust particles was validated and  
91 the role that East Asian dust plays in the ice nucleation process in the atmosphere was further investigated.

92 The remainder of the manuscript is presented as follows. Section 2 provides a description of the model including, and  
93 the implementation work for coupling the aerosol-aware Thompson-Eidhammer microphysics scheme and the  
94 GOCART aerosol model in WRF-Chem is elaborated in Section 3, followed by the model configurations for numerical  
95 simulations in section 4.3. Section 5.4 presents the observational data used to validate the performance of the GOCART-  
96 Thompson microphysics scheme. Section 6.5 is the results and discussion, followed by the conclusions in section 7.6.

97

## 98 **2 Model description**

99 WRF-Chem is an online-coupled regional modeling system, which means that it can simultaneously simulate the  
100 meteorological field, the chemical field, and the interactions in between (Grell et al., 2013). The chemical model  
101 contains several gas- and aerosol-phase chemical schemes. In this study, we focus on the GOCART model, a simple  
102 aerosol model that will be used for dust simulation.

103

### 104 **2.1 GOCART aerosol model**

105 GOCART is an aerosol model for simulating major tropospheric natural-source aerosol components, such as sulfate,  
106 mineral dust, black carbon, organic carbon, and sea-salt aerosols (Ginoux et al., 2001;Chin et al., 2000). It has been  
107 implemented into WRF-Chem as a bulk aerosol scheme. GOCART is a simple aerosol scheme that can predict the  
108 mass of aerosol components, but does not account for complex chemical reactions. Therefore, it is numerically  
109 efficient in simulating aerosol transport, and thus applicable to cases without many chemical processes, especially  
110 dust events. Typically it requires 40% to 50% more computational time by applying WRF-Chem run with GOCART  
111 aerosol model than the standard WRF to produce the same period of simulation.

112 Shao's dust emission scheme -model (Kang et al., 2011;Shao, 2004, 2001;Shao et al., 2011) is one of the dust emission  
113 schemes in the GOCART aerosol model, and has been demonstrated to exhibit superior performance in reproducing

114 the dust cycle over East Asia compared to other emission schemes (Su and Fung, 2015). The Shao's emission scheme  
115 was updated in WRF-Chem since version 3.8 released in 2016 to produce five size bins for dust emission, with  
116 diameters of  $< 2 \mu\text{m}$ ,  $2\text{--}3.6 \mu\text{m}$ ,  $3.6\text{--}6.0 \mu\text{m}$ ,  $6.0\text{--}12.0 \mu\text{m}$ , and  $12.0\text{--}20.0 \mu\text{m}$ , and mean effective radii of  $0.73 \mu\text{m}$ ,  
117  $1.4 \mu\text{m}$ ,  $2.4 \mu\text{m}$ ,  $4.5 \mu\text{m}$ , and  $8.0 \mu\text{m}$ .

118

## 119 **2.2 Thompson-Eidhammer microphysics scheme**

120 The Thompson microphysics scheme is a bulk two-moment aerosol-aware microphysics scheme that considers the  
121 mixing ratios and number concentrations for five water species: cloud water, cloud ice, rain, snow and a hybrid  
122 graupel/hail category (Thompson et al., 2004). The updated Thompson-Eidhammer scheme is an aerosol-aware  
123 version of the Thompson scheme (Thompson and Eidhammer, 2014), which incorporates the activation of aerosols  
124 acting as cloud condensation nuclei and IN, and therefore it explicitly predicts the number concentrations of CCN  
125 and IN, as well as the number concentrations of cloud droplets and ice crystals. Hygroscopic aerosols that serve as  
126 cloud condensation nuclei are referred to as water-friendly aerosols, and those non-hygroscopic ice-nucleating  
127 aerosols are referred to as ice-friendly aerosols. The cloud droplets nucleate from explicit aerosol number  
128 concentrations using a look-up table for the activated fraction as determined by the predicted temperature, vertical  
129 velocity, number of available aerosols, and pre-determined values of the hygroscopicity parameter and aerosol mean  
130 radius.

131 In the Thompson-Eidhammer scheme, the ice nucleation process is triggered once the relative humidity with respect  
132 to ice ( $RH_i$ ) exceeds 105%. Furthermore, when the relative humidity with respect to water ( $RH_w$ ) is above 98.5%, it  
133 is counted as condensation and immersion freezing, and calculated by DeMott's parameterization scheme (DeMott et  
134 al., 2010); when  $RH_w$  is below 98.5%, it is treated as deposition nucleation, and determined by the Phillips'  
135 parameterization scheme (Phillips et al., 2008). Both DeMott's scheme and Phillips' scheme are coupled with  
136 concentration of ice-friendly aerosols. In addition, the freezing of deliquesced aerosols using the hygroscopic aerosol  
137 concentration is parameterized following Koop's parameterization scheme (Koop et al., 2000), and it is coupled with  
138 concentration of water-friendly aerosols.

139 The DeMott's parameterization scheme for determining the condensation and immersion freezing in the Thompson-  
 140 Eidhammer microphysics scheme was proposed in 2010 (DeMott et al., 2010, hereafter referred to as the DeMott2010  
 141 scheme) based on combined data from field experiments at a variety of locations over 14 years. In the Demott2010  
 142 parameterization, the relationship between the number concentration of aerosol-friendly aerosols and ice nucleating  
 143 particles (INP) is as follows: **2.2 Aerosol-aware Thompson microphysics scheme**

$$n_{IN,T_k} = a(273.16 - T_k)^b n_{aero}^{(c(273.16 - T_k) + d)} \quad (1)$$

145 where  $n_{IN,T_k}$  is the ~~ice crystal~~INP number concentration at temperature of  $T_k$ ;  $n_{aero}$  is the number concentration of  
 146 ice-friendly aerosols, and  $a$ ,  $b$ ,  $c$ , and  $d$  are constant coefficients equal to  $5.94 \times 10^{-5}$ , 3.33,  $2.64 \times 10^{-2}$ , and  $3.33 \times 10^{-3}$ ,  
 147 respectively. The parameterization was tested with various temperatures and number concentration of ice-friendly  
 148 aerosols, yielding a good performance in reproducing ice crystal number concentration under conditions of relatively  
 149 low mixing ratio of water vapor or low concentration of INP compared with field-experimental data. The relationship  
 150 between the simulated number concentrations of ice-friendly aerosols and INP is basically linear for concentrations  
 151 of both of under  $1,000 \text{ \#/cm}^3$  (DeMott et al., 2010).

152 The above parameterization was further developed in 2015 (DeMott et al., 2015, hereafter the DeMott2015 scheme)  
 153 for conditions of higher mixing ratio of water vapor or higher concentrations of ice crystals based on the latest data  
 154 from field and laboratory experiments. According to the updated observational data, INP concentration increases  
 155 exponentially with number concentration of ice-friendly aerosols, and existing aerosols with relatively low  
 156 concentrations (less than  $1,000 \text{ \#/cm}^3$ ) can produce a large number of INP (more than  $100,000 \text{ \#/cm}^3$ ). The updated  
 157 relationship between the number concentrations of ice-friendly aerosols and INP in the DeMott2015 parameterization  
 158 scheme is as follows.

$$n_{IN,T_k} = c_f n_{aero}^{\alpha(273.16 - T_k) + \beta} \exp(\gamma(273.16 - T_k) + \delta) \quad (2)$$

160 where  $\alpha$ ,  $\beta$ ,  $\gamma$ , and  $\delta$  are constant coefficients equal to 0, 1.25, 0.46, and -11.6, respectively. The calibration factor  $c_f$   
 161 ranges from 1 to 6, and is recommended to be 3.

162 The number concentration of INP produced by the DeMott2015 scheme is much higher than that produced by the  
 163 DeMott2010 scheme, and the difference grows larger with decreasing temperature and increasing number  
 164 concentration of ice-friendly aerosols (DeMott et al., 2015). ~~As the DeMott2015 scheme has been examined using~~

165 ~~more comprehensive field—and laboratory—experimental data, we apply the DeMott2015 ice nucleation scheme in the~~  
166 ~~be used without modifying the code. Instead of using the DeMott2010 scheme by default, we modified the code to~~  
167 ~~call the DeMott2015 scheme in Thompson-Eidhammer scheme for the condensation and immersion freezing in our~~  
168 ~~simulations for investigating the, instead of the DeMott2010 scheme, in the default aerosol-aware Thompson-~~  
169 ~~Originally, the calibration factor  $c_f$  is set to be 3; the threshold temperature is set to be  $-20$  °C. For the Thompson-~~  
170 ~~Eidhammer scheme ice nucleation process in Thompson-Eidhammer scheme WRF-Chem, the number concentrations~~  
171 ~~of both water-friendly aerosols and ice-friendly aerosols are pre-given in the initialization of the simulations, and are~~  
172 ~~derived from the climatological data produced by global model simulations in which particles and their pre cursors are~~  
173 ~~emitted by natural and anthropogenic sources and explicitly modeled with various size bins for multiple species of~~  
174 ~~aerosols by the GOCART model. In the consequent simulations, a fake aerosol emission is implemented by giving a~~  
175 ~~variable lower boundary condition based on the initial near-surface aerosol concentration and a simple mean surface~~  
176 ~~wind for calculating a constant aerosol flux at the lowest level in the model. The number concentrations of both water-~~  
177 ~~friendly aerosols and ice-friendly aerosols are then updated at every time step by summing up the fake aerosol emission~~  
178 ~~fluxes and tendencies induced by aerosol-cloud-interactions. The limitation of the current aerosol-aware Thompson-~~  
179 ~~Eidhammer scheme is that the aerosol profile generated from a fake emission cannot represent the realistic aerosol~~  
180 ~~level all the time, especially over areas with complex weathers, such as East Asia, leading to errors in quantifying the~~  
181 ~~indirect effects of aerosols. Originally, the calibration factor  $c_f$  is set to be 3; the threshold temperature is set to be—~~  
182 ~~20 °C. The ice nucleation process is triggered once the relative humidity with respect to ice (RH<sub>i</sub>) exceeds 105%.~~  
183 ~~Furthermore, when the relative humidity with respect to water (RH<sub>w</sub>) is above 98.5%, it is counted as condensation~~  
184 ~~and immersion freezing, and calculated by DeMott2015 scheme; when RH<sub>w</sub> is below 98.5%, it is treated as deposition~~  
185 ~~nucleation, and determined by the parameterization of Phillips et al. (Phillips et al., 2008) is applied to account for~~  
186 ~~deposition nucleation.~~

187 By coupling the GOCART aerosol model with the Thompson-Eidhammer microphysics scheme, it allows the model  
188 to explicitly evaluate the indirect effect of natural-source aerosols on the basic of a relatively realistic emission  
189 production, for instance, the effect of dust on ice nucleation during severe dust episodes or dust-intensive season.

190

### 191 3 Implementation of GOCART-Thompson microphysics scheme

192 To investigate the real-time indirect effects of dust aerosol over East Asia, a new treatment was implemented into  
193 WRF-Chem to couple the GOCART aerosol model and the Thompson-Eidhammer microphysics scheme, namely  
194 GOCART-Thompson microphysics scheme. To accomplish this, WRF-Chem version 3.8.1 has been modified in the  
195 following three steps.

196

### 197 **3.1 Upgraded GOCART aerosol model**

198 Currently, the GOCART aerosol model generates only the mass concentration for aerosols but no number  
199 concentrations. However, the number concentrations of aerosols are required for a microphysics scheme to evaluate  
200 the indirect effects of aerosols. Therefore, modification was needed to provide information about the number  
201 concentrations of aerosols from the mass concentration produced in GOCART aerosol model.

202 The aerosol mass concentration was converted into number concentration using the aerosol density and effective radius  
203 for each size bin. Assuming that dust particles are spherical, the mass per dust particle ( $m_p$ ,  $\mu\text{g}/\#$ ) for a size bin can  
204 be approximated through the mean effective radius ( $r_{dust}$ , m) and density ( $\rho_{dust}$ ,  $\text{kg}/\text{m}^3$ ) for that size bin.

$$205 \quad m_p = \rho_{dust} \times \frac{4}{3} \times \pi r_{dust}^3 \quad (3)$$

206 The number concentration of dust particles  $N$  ( $\#/\text{kg}$ ) for size bin  $n$  at a grid point  $(i, j, k)$  is then calculated by the  
207 following equation:

$$208 \quad N(i, j, k, n) = C(i, j, k, n) / m_p \quad (4)$$

209 where  $C(i, j, k, n)$  is the dust mass mixing ratio ( $\mu\text{g}/\text{kg}$ ) for size bin  $n$  at grid point  $(i, j, k)$ . Summing up the aerosol  
210 number concentrations through all of the size bins gives a total dust number concentration, which will be passed into  
211 the Thompson-Eidhammer microphysics scheme. Note that all of the dust particles are treated as ice-friendly aerosols  
212 in this study and represented by a newly-introduction variable, ice -friendly aerosol produced by GOCART aerosol  
213 model (*GNIFA*).

$$214 \quad GNIFA(i, j, k) = \sum_{n=1}^n N(i, j, k, n) \quad (5)$$

215

216 **3.2 GOCART-Thompson microphysics scheme**

217 This part of modification was to hoop up the GOCART aerosol model and the Thompson-Eidhammer microphysics  
218 scheme.

219 Instead of reading in the pre-given climatological aerosol data, the initialization module of the Thompson-Eidhammer  
220 microphysics scheme was modified to apply the bulk number concentration of ice-friendly aerosols produced by the  
221 GOCART aerosol model for the calculation of the number concentration of ice nucleating particles.

222 After the microphysical processes are finished for a particular time step, the tendency of the bulk aerosol number  
223 concentration ( $ten_{dust}$ , #/kg/s) produced by the microphysics scheme is then passed into a wet scavenging scheme,  
224 which will be described in detail in the following subsection, for the model to calculate the loss of aerosol mass due  
225 to the microphysical processes within clouds, and update the aerosol mass field.

226

227 **3.3 In-cloud wet scavenging**

228 As no in-cloud scavenging is considered for dust aerosol in WRF-Chem, a new wet scavenging process was introduced  
229 into WRF-Chem to calculate the loss of aerosol mass due to the microphysical processes within clouds using the  
230 tendency of aerosol number concentration produced by the microphysics scheme. Assuming that the collection of dust  
231 particles is proportional to the number concentration of dust particles, the fraction of dust particle for each size bin  
232 ( $\phi$ , %) can be calculated in the GOCART aerosol model:

233 
$$\phi(i, j, k, n) = \frac{N(i, j, k, n)}{GNIFA(i, j, k)} \quad (6)$$

234 The tendency of ice-friendly aerosol is then distributed into each size bin and the loss of dust mass due to the  
235 microphysical processes ( $wetscav$ ,  $\mu g/kg$ ) for a particular size bin  $n$  is calculated by the following equation:

236 
$$wetscav(i, j, k, n) = ten_{dust}(i, j, k) \times \phi(i, j, k, n) \times m_p \times dt \quad (7)$$

237 where  $dt$  is the time step for the simulation.

238 The mass mixing ratio ( $C$ ,  $\mu g/kg$ ) for dust aerosol in a particular size bin  $n$  is then updated at the next time step:



239 
$$C_{(i,j,k,n)}^{t+1} = C_{(i,j,k,n)}^t - wetscav_{(i,j,k,n)}^t \quad (8)$$

240 Apart from the in-cloud scavenging, the below-cloud wet removal is calculated by the default wet deposition scheme  
241 in the GOCART aerosol model, in which the wet removal of dust is removed by a constant scavenging factor when  
242 there is a precipitation (Duce et al., 1991; Hsu et al., 2009).

243

#### 244 4 Model configurations

245 A numerical experiment was ~~conducted~~conducted to examine the performance of the newly-implemented GOCART-  
246 Thompson microphysics scheme in simulating the ice nucleation process induced by dust in the atmosphere. Two  
247 simulations were ~~conducted~~carried out for the numerical test. One control run (CTRL) was ~~conducted~~simulated  
248 without dust and one test run (DUST) ~~was conducted~~ with dust. According to the observations, the dust events in 2012  
249 over East Asia were concentrated in mid-March to late-April, and the satellite observations from mid-March to the  
250 end of April were available for model validation; therefore, the simulation period was from March 9 to April 30, 2012,  
251 with the first eight days as “spin-up” time. Only the results from March 17 to April 30, 2012 were used for the analysis.  
252 The final reanalysis data provided by the United States National Center of Environmental Prediction with a horizontal  
253 resolution of one degree was used for generating the initial and boundary conditions for the meteorological fields, and  
254 the simulations were re-initialized every four days, with the aerosol field being re-cycled, which means that the output  
255 of the aerosol field from the previous four-day run was used as the initial aerosol state for the subsequent four-day  
256 run. The integration time step for the simulations was 90s.

257 Two nested domains were used for the simulations, as shown in Figure 1. The outer domain (domain 1) is in a  
258 horizontal resolution of 27 km and covers the entire East Asia region. The inner domain (domain 2) is in a horizontal  
259 resolution of 9 km and covers the entire central to East China. Both domains have 40 vertical layers, with the top layer  
260 at 50 hPa. The locations of the two major dust sources, the Taklimakan Desert (TD) and the Gobi Desert (GD), are  
261 marked in Figure 1.

262 In the GOCART-Thompson scheme, the deposition nucleation is determined by the Phillip’s parameterization  
263 (Phillips et al., 2008), the freezing of deliquesced aerosols using the hygroscopic aerosol concentration is  
264 parameterized following Koop’s parameterization scheme (Koop et al., 2000), and the condensation and immersion

265 ~~freezing is parameterized by the DeMott2015 ice nucleation scheme. The new wet scavenging scheme was used for~~  
266 ~~in-cloud wet scavenging of aerosols due to microphysical processes.~~ The GOCART aerosol model was applied to  
267 simulate aerosol processes (Ginoux et al., 2001;Ginoux et al., 2004). ~~and produce the number concentration of dust~~  
268 ~~particles in DUST.~~ Shao's dust emission (Kang et al., 2011;Shao et al., 2011) with soil data from the United states  
269 Geological Survey (Soil Survey Staff, 1993), which have been demonstrated to have good performance in reproducing  
270 dust emissions over East Asia, was used to generate dust emission in the ~~test-rusimulations of TESTa.~~ ~~The number~~  
271 ~~concentration of dust particles was then fed into the GOCART-Thompson microphysics scheme and treated as ice-~~  
272 ~~friendly aerosols for calculating the condensation and immersion freezing involving dust by DeMott2015~~  
273 ~~parameterization scheme. In addition, the pre-given climatological profiles applied in the original Thompson-~~  
274 ~~Eidhammer scheme (Thompson and Eidhammer, 2014) were used to provide the number concentration of water-~~  
275 ~~friendly aerosols for the freezing of deliquesced aerosols calculated by Koops's parameterization scheme to consider~~  
276 ~~the background indirect effect of aerosols on ice nucleation for both the simulations of both CTRL and DUST in this~~  
277 ~~study. No other aerosol emissions were considered in the simulations. The newly implemented GOCART Thompson~~  
278 ~~microphysics scheme.(Thompson and Eidhammer, 2014) In the GOCART Thompson scheme, the deposition~~  
279 ~~nucleation is determined by the parameterization of Phillips et al. (Phillips et al., 2008), the freezing of deliquesced~~  
280 ~~aerosols using the hygroscopic aerosol concentration is parameterized following Koop et al. (Koop et al., 2000), with~~  
281 ~~the background aerosol concentration set to be  $1/L$ , and the condensation and immersion freezing is parameterized by~~  
282 ~~the DeMott2015 ice nucleation scheme. The new wet scavenging scheme was used for in-cloud wet scavenging of~~  
283 ~~aerosols due to microphysical processes.~~

284 Other important physical and chemical parameterizations applied for the simulations are as follows. The Mellor–  
285 Yamada–Janjic (MYJ) turbulent kinetic energy scheme was used for the planetary boundary layer parameterization  
286 (Janjić, 2002, 1994); the moisture convective processes were parameterized by the Grell-Freitas scheme (Grell and  
287 Freitas, 2014); the short-wave (SW) and long-wave (LW) radiation budgets were calculated by the Rapid Radiative  
288 Transfer Model for General Circulation (RRTMG) SW and LW radiation schemes (Mlawer et al., 1997;Iacono et al.,  
289 2008); the gravitational settling and surface deposition were combined for aerosol dry deposition calculation (Wesely,  
290 1989); a simple washout method was used for the below-cloud wet deposition of aerosols (Duce et al., 1991;Hsu et  
291 al., 2006); and the aerosol optical properties were calculated based on the volume-averaging method (Horvath, 1998).

292

## 293 **5 Observations**

### 294 **5.1 Surface PM<sub>10</sub> observations**

295 The hourly observations of surface concentration of particulate matter with diameter smaller than 10  $\mu\text{m}$  (PM<sub>10</sub>) at ten  
296 environmental monitoring stations located in or surrounding the dust source areas in East Asia were used to examine  
297 the capability of the model in reproducing dust levels at the ground surface during the simulation period. The ten  
298 stations (indicated by blue dots in Figure 1) were located in the following five cities: Jinchang, Gansu Province,  
299 Yinchuan, Qinghai Province, Shizuishan, Ningxia Province, Baotou, Inner Mongolia, and Yan'an, Shaanxi Province,  
300 with two stations in each city.

301

### 302 **5.2 AERONET AOD observations**

303 The AERONET program is a ground-based aerosol remote sensing network for measuring aerosol optical properties  
304 at sites distributed around the globe. This program provides a long-term database of aerosol optical properties such as  
305 aerosol extinction coefficient, single-scattering albedo, and aerosol optical depth (AOD) measured at various  
306 wavelength. The observational data from two sites were available for comparison with the simulation results during  
307 the simulation period in this study. One was Dalanzadgad located to the north of the Gobi Desert in Mongolia, and  
308 the other was the Semi-Arid Climate and Environment Observatory of Lanzhou University (SACOL) located at  
309 Lanzhou, Gansu Province, China. The exact locations of the two AERONET sites are depicted by the red triangles in  
310 Figure 1. All of the measured data had passed the quality control standard level 2, with an uncertainty of  $\pm 0.01$  (Holben  
311 et al., 2001).

312

### 313 **5.3 Satellite data**

#### 314 **5.3.1 Multi-angle Imaging SpectroRadiometer (MISR)**

315 The MISR instrument aboard the Terra platform of the United State National Aeronautics and Space Administration  
316 (NASA) has been monitoring aerosol properties globally since 2000. It measures the aerosol properties in four narrow

317 spectral band centered at 443 nm, 555 nm, 670 nm, and 865 nm, due to which the aerosol properties even over highly  
318 bright surfaces, such as deserts, can be retrieved (Martonchik et al., 2004;Diner et al., 1998). In this study, the AOD  
319 data at 555 nm retrieved from the MISR level 3 products with a spatial resolution of 0.5° were used for comparison  
320 with the spatial distribution of simulated AOD over East Asia during the investigated period.

321

### 322 **5.3.2 Moderate Resolution Imaging Spectroradiometer (MODIS)**

323 The MODIS instruments aboard Terra and Aqua platforms of NASA monitor Earth's surface and provide global high-  
324 resolution cloud and aerosol optical properties at a near-daily interval (Kaufman et al., 1997).

325 To retrieve aerosol information over bright surfaces, the Deep Blue algorithm was developed to employ retrievals  
326 from the blue channels of the MODIS instruments, at which wavelength the surface reflectance is very low, such that  
327 the presence of aerosol can be detected by increasing total reflectance and enhanced spectral contrast (Hsu et al., 2006).

328 By applying this algorithm, the AOD values at wavelengths of 214 nm, 470 nm, 550 nm, and 670 nm over bright  
329 surfaces can be retrieved. In this study, the MODIS level 2 AOD data at 550 nm with a spatial resolution of 10 km  
330 were used for comparison with the simulated AOD during the simulation period.

331

### 332 **5.3.3 Cloud-Aerosol Lidar and Infrared Pathfinder Satellite Observation (CALIPSO)**

333 The Cloud-Aerosol Lidar and Infrared Pathfinder Satellite, which is aboard the Aqua platform of NASA, combines  
334 an active Light Detection and Ranging (LIDAR) instrument with passive infrared and visible imagers to probe the  
335 vertical structure and properties of thin clouds and aerosols around the globe (Vaughan et al., 2004). It aims to fill  
336 existing gaps in the ability to measure the global distribution of aerosols and cloud properties, and provides three-  
337 dimensional perspectives of how clouds and aerosols form, evolve, and affect weather and climate. It measures high-  
338 resolution vertical profiles of aerosol and cloud extinction coefficient globally at wavelengths of 532 nm and 1064 nm.

339 The atmospheric IWC is derived from the observational cloud extinction coefficients at 532 nm (Winker et al., 2009).

340 In this study, the vertical profiles of CALIPSO IWC with a horizontal resolution of 5 km and vertical resolution of 60  
341 m were applied to verify the performance of the model in simulating the vertical distribution of atmospheric IWC.

342

## 343 6 Results and model validation

### 344 6.1 Dust over East Asia

345 The time series of daily average dust load over the entire East Asia region (domain 1) during the simulation period is  
346 shown in Figure 2a. In total four dust events occurred during the simulation period, lasting from March 18 to 25,  
347 March 30 to April 7, April 9 to 19, and April 22 to 29, 2012. The case from April 22 to 29 was the most significant  
348 one, with daily dust load that double as the other cases. The fraction of daily dust load for each size bin is also shown  
349 in Figure 2a. The dust particles in the fourth and fifth bins with effective diameters ranging from 6 to 20  $\mu\text{m}$  account  
350 for the major part (around 60%) of the total mass of dust aerosols, ~~and dust particles with diameters smaller than 6  $\mu\text{m}$~~   
351 ~~account for around 40% of the total mass of dust aerosols.~~

352 The number concentrations of dust particles over East Asia were vertically integrated to obtain the number density of  
353 dust particles. As shown in Figure 2b, the time series of the daily average number density of dust particles over East  
354 Asia during the simulation period shows a similar distribution as that for dust load; the noteworthy distinction between  
355 the two time series lies in the fraction of each size bin. The two size bins with the smallest diameters (no larger than  
356 3.6  $\mu\text{m}$ ) account for over 80% of the total number of dust particles, and the particles with diameters smaller than 6  $\mu\text{m}$   
357 account for over 95% of the total number of dust particles, indicating that the smallest dust particles are the main  
358 source of ice-friendly aerosol to serve as IN in the atmosphere.

359

#### 360 6.1.1 Surface $\text{PM}_{10}$ concentration

361 To evaluate the performance of WRF-Chem in reproducing dust emissions over East Asia, the simulated surface  $\text{PM}_{10}$   
362 concentrations were compared with the observations from the ten environmental monitoring stations located near dust  
363 sources and downwind areas (described in Section 5.1). The time series of the observed and simulated surface  $\text{PM}_{10}$   
364 concentrations during the simulation period are shown in Figure 3. Note that the simulated  $\text{PM}_{10}$  concentrations were  
365 extracted from the nearest grid point to the geographical coordinates of the stations. The stations in the same city were  
366 assigned into one group, ~~thus-such that~~ there were five groups in Figure 3. Overall, the model shows a good  
367 performance in simulating the dust cycle at different locations, with evolution and magnitude of the daily mean  $\text{PM}_{10}$

368 concentration well captured at most of the stations. The model tends to produce lower surface PM<sub>10</sub> concentration  
369 than those observed, as no other emissions were considered in the simulations apart from dust. However, the dust  
370 events on March 21 and April 26 were overestimated by the model at one station in Jinchang (Figure 3e), both stations  
371 in Shizuishan (Figure 3c and d) and Yinchuan (Figure 3i and j).

372 The performance statistics were computed from the daily average simulated PM<sub>10</sub> concentration from DUST and the  
373 corresponding observations, as shown in Table 1. The model tends to produce lower surface PM<sub>10</sub> concentrations than  
374 those observed, as no other emissions were considered in the simulations. The mean bias (MB) ranged from -108.73  
375  $\mu\text{g}/\text{m}^3$  to 72.46  $\mu\text{g}/\text{m}^3$ , with a mean over all the stations of -18.84  $\mu\text{g}/\text{m}^3$ . The mean error (ME) ranged from 46.07  
376  $\mu\text{g}/\text{m}^3$  to 155.83  $\mu\text{g}/\text{m}^3$ , with a mean over all of the stations of 107.24  $\mu\text{g}/\text{m}^3$ . The root mean squared error (RMSE)  
377 ranged from 64.78  $\mu\text{g}/\text{m}^3$  to 317.73  $\mu\text{g}/\text{m}^3$ , with a mean over all of the stations of 181.28  $\mu\text{g}/\text{m}^3$ . The relatively large  
378 values of the MB, ME and RMSE are mainly attributed to the fact that no other aerosol emissions were considered in  
379 the simulations other than dust, while the surface PM<sub>10</sub> concentration at the monitoring stations is influenced by  
380 aerosols emitted from other sources, such as anthropogenic emissions. The correlation coefficient (r) ranged from 0.59  
381 to 0.87, with an average for all of the stations of 0.70. The comparisons between the observed and simulated surface  
382 PM<sub>10</sub> concentration indicates that the model is capable of reproducing the surface dust concentration reasonably during  
383 dust events over East Asia.

384

#### 385 **6.1.2 AOD time series**

386 To examine the performance of the model in reproducing the column sum of dust in the atmosphere, the simulated  
387 AOD values were compared with observations measured at two AERONET sites during the simulation period, as  
388 shown in Figure 4.

389 The site at Dalanzadgad (Figure 4a) is located in Mongolia to the north of the Gobi Desert. Overall, the evolution and  
390 magnitude of the AOD time series at Dalanzadgad were reasonably reproduced by the model during the simulation  
391 period, despite the fact that the simulated AOD was overestimated at the end of March and in mid-April compared to  
392 the observed values.

393 SACOL (Figure 4b) is a site located in Lanzhou, Gansu Province, which is a typical downwind area for dust in China.  
394 The model showed a good performance in reproducing the time series of AOD at SACOL during the entire simulation  
395 period, with evolution and magnitude of AOD well captured.

396

### 397 6.1.3 AOD spatial distribution

398 The spatial distribution of monthly mean simulated AOD was also compared with observed values from MODIS and  
399 MISR products [in Figure 5](#). Note that the high AOD values observed at North, East, South China and part of Southeast  
400 Asia are attributed to the abundant anthropogenic emissions, while those high values in the circle area are mostly due  
401 to dust events. The region with high AOD values in the west part of the circled area is TD, and the region with  
402 relatively lower AOD in the east part of the circled area is GD. The AOD observed by MODIS showed high values at  
403 the dust source region in both March and April of 2012, as shown in Figures 5a and b. The mean observed AOD over  
404 GD was lower than that over TD in both March and April, and the mean observed AOD was higher in April than in  
405 March over both dust source areas. The spatial patterns of AOD observed by MISR are similar to MODIS, with  
406 comparable mean values over GD. However, the mean AOD values over TD observed by MISR are 36% and 40%  
407 lower than those by MODIS, [respectively in March and April, respectively](#) (Figure 5c and d).

408 The spatial patterns for the mean simulated AOD were similar to the observed values in both months but closer to  
409 those from MODIS, as shown in Figures 5e and f. The model shows a good capability in capturing the spatial  
410 characteristics of the AOD over the dust source areas. For example, the mean observed AOD was higher in the  
411 southern part of TD than that in the northern part in March, and showed an increase from March to April over GD,  
412 both of which were captured by the model. The values of the mean simulated AOD over the Gobi Desert (0.33 for  
413 March and 0.39 for April) are comparable to the observational values from both MODIS (0.30 for March and 0.32 for  
414 April) and MISR (0.31 for March and 0.34 for April), but the mean simulated AOD over TD (0.54 for March and 0.64  
415 for April) are between the values of the MISR observations (0.72 for March and 0.88 for April) and the MODIS  
416 observations (0.46 for March and 0.53 for April).

417 In summary, it was demonstrated that the dust emissions simulated by WRF-Chem are reliable for further analysis by  
418 the comparison between the simulation results and the observations for surface PM<sub>10</sub> concentrations, as well as the  
419 temporal and spatial distributions of AOD values.

420

## 421 6.2 Cloud ice over East Asia

422 Dust particles are effective IN and play an important role in ice nucleation in the atmosphere under appropriate  
423 conditions. With the large number of IN served by dust particles emitted into the atmosphere, an increase in the number  
424 of ice crystals is expected in the results from DUST compared with those from CTRL, after taking into account the  
425 effects of dust particles in the GOCART–Thompson microphysics scheme. Figure 6 shows the overall comparison  
426 between the simulated cloud ice mixing ratio and ice crystal number concentration at each simulated data point (at  
427 all model grids at hourly intervals) from CTRL and DUST during the entire simulation period.

428 As expected, the model produces a much higher cloud ice mixing ratio (Figure 6a) and ice crystal number  
429 concentration (Figure 6b) in DUST. The simulated cloud ice mixing ratio produced in CTRL is lower than 2 μg/kg at  
430 most data points during the simulation period, whereas the data points with simulated ice mixing ratio higher than 2  
431 μg/kg are substantially increased in the output of DUST. Similarly, the simulated ice crystal number concentration  
432 produced in CTRL is lower than  $0.5 \times 10^6$  #/kg at most data points during the simulation period, by contrast, the  
433 simulated ice crystal number concentration number concentration is higher than  $0.5 \times 10^6$  #/kg at over a half of total  
434 data points in DUST. The substantial increase of simulated cloud ice mixing ratio and ice crystal number concentration  
435 indicates that the enhancement of ice nucleation process induced by dust is successfully reproduced by the newly-  
436 implemented GOCART-Thompson microphysics scheme during the simulation period. ±

437

### 438 6.2.1 Spatial distribution of ice water path (IWP)

439 The spatial distributions of the simulated IWP and ice crystal number density from CTRL and DUST in Figure 7  
440 further demonstrate the enhancement in cloud ice due to dust over East Asia. The IWP produced by CTRL was ~~lower~~  
441 ~~than 1 g/m<sup>2</sup> over the entire East Asia Region~~ relatively high over west and east China, as well as at the south boundary  
442 of the simulation domain, with the values as high as 20 g/m<sup>2</sup> (Figure 7a). After considering the effect of dust in the



443 ice nucleation process, the IWP produced by DUST increased substantially ~~over the entire region, especially~~ over dust  
444 ~~, with values as high as 10 g/m<sup>3</sup> (Figure 7b and c), with values higher by 5-10 g/m<sup>2</sup>.~~ The mean IWP averaged over the  
445 period was ~~9.159.33~~ 9.159.33 g/m<sup>2</sup> for DUST, and ~~0.707.95~~ 0.707.95 g/m<sup>2</sup> for CTRL. As shown in Figures 7d–f, the spatial pattern for  
446 enhancement of ice crystal number density over East Asia was similar with that for the IWP. The mean ice crystal  
447 number density averaged over the domain during the simulation period was ~~2.9179~~ 2.9179 × 10<sup>8</sup> /m<sup>2</sup> for DUST, and  
448 /m<sup>2</sup> for CTRL.

449 The mean IWP and ice crystal number density were increased by ~~more than one order of magnitude~~ 15% and 8% over  
450 vast areas of East Asia upon considering the effect of dust in the ice nucleation process in the simulation, and such  
451 effect can reach as far as ~~the open ocean of the South China Sea at the southern part of the simulation domain~~ Western  
452 Pacific (Figure 7b and 7e), ~~as~~. ~~During dust season,~~ the outbreak of cold high system over northeast Asia can bring  
453 quantitative dust aerosol down to ~~the the South China Sea~~ Western Pacific or even further during dust season. ~~In such~~  
454 ~~cases, strong northwestlies swept across the entire China, and brought large amount of dust, especially fine particles,~~  
455 ~~from source areas to the south border of the domain. Besides, the water vapor mixing ratio over South China Sea can~~  
456 ~~be several times as that over north China. Large amount of ice nuclei transported by winds, combining with abundant~~  
457 ~~water vapor, results in a substantial enhancement in the formation of ice crystals over the area at the southern part of~~  
458 ~~the simulation domain. The larger fraction of fine particles in the dust plumes that reach this area results in a much~~  
459 ~~higher enhancement of ice crystal number concentration than the mass of ice crystals.~~

460

#### 461 6.2.2 IWC during dust events

462 The vertical profile of the simulated IWC was also compared with the observation from CALIPSO during dust events.  
463 As mentioned in section 5.1, a total of four dust events occurred during the simulation period, lasting from March 18  
464 to 25, March 30 to April 7, April 9 to 19, and April 22 to 28, 2012. As shown in Figures 8 and 9, the performance of  
465 the model in simulating the vertical profile of IWC was evaluated by comparing the observations measured at 06 UTC  
466 on March 21, 18 UTC on April 1, 18 UTC on April 9, and 05 UTC on April 23, 2012 with the simulated profiles at  
467 the same hour.

468 CALIPSO measures the global distribution of aerosol and cloud properties by LIDAR, which uses a laser to generate  
469 visible light with a wavelength of 1  $\mu\text{m}$  or less to detect small particles or droplets in the atmosphere. Therefore,  
470 CALIPSO instruments are more sensitive to tenuous ice clouds and liquid clouds composed of small particles or  
471 droplets, which are invisible to instruments using signals of near-infrared or infrared wavelength to detect clouds.  
472 Moreover, the LIDAR signal is attenuated rapidly in optically dense clouds that the infrared or near-infrared signals  
473 can easily penetrate (Winker et al., 2010). As a result, the CALIPSO observations of IWC are mostly at the locations  
474 where the temperatures is lower than  $-40\text{ }^{\circ}\text{C}$  and the altitude is greater than 6 km poleward to 12 km equatorward,  
475 and mostly those without precipitating ice. Given the above considerations, the simulated IWC profiles compared with  
476 the CALIPSO observations are referred to as only cloud ice in this section.

477 The simulated dust load over East Asia at 06 UTC on March 21, 2012 is shown in Figure 8a, in which the dust covered  
478 vast areas from West to East China between  $35^{\circ}\text{N}$  and  $45^{\circ}\text{N}$ , and the orbit of the satellite passed through the area with  
479 heavy dust load at around  $100^{\circ}\text{E}$ . Along the satellite orbit, the abundant dust particles were transported to as high as  
480 10 km aloft (Figure 8c). At this time, a high concentration of IWC was observed along the satellite orbit at an altitude  
481 of around 10 km between  $30^{\circ}\text{N}$  and  $45^{\circ}\text{N}$  (Figure 8e). The simulation result from CTRL (Figure 8g) shows that the  
482 model produces some ice cloud at altitude of 9–10 km between  $35^{\circ}\text{N}$  and  $45^{\circ}\text{N}$ , but with much lower IWC compared  
483 to the observations. Nevertheless, by considering the effect of dust on ice nucleation process in DUST, it results in a  
484 much higher IWC at altitude of 9–10 km between  $35^{\circ}\text{N}$  and  $45^{\circ}\text{N}$  (Figure 8i), which is much more consistent with the  
485 observations. The comparison between the simulation results from CTRL and DUST indicates that the high IWC  
486 observed by the satellite between  $30^{\circ}\text{N}$  and  $35^{\circ}\text{N}$  might be unrelated to microphysical processes, but instead due to  
487 strong convective motions over South China.

488 On April 1, 2012, Central to East China was covered by a thick dust plume, and the orbit of the satellite passed between  
489  $25^{\circ}\text{N}$  and  $43^{\circ}\text{N}$  along  $120^{\circ}\text{E}$  at 18 UTC (Figure 8b). Dust particles were distributed vertically from the surface to over  
490 8 km along the satellite orbit (Figure 8d). A band of high IWC was observed by the satellite at altitude of 5 km to 10  
491 km between  $33^{\circ}\text{N}$  and  $44^{\circ}\text{N}$  (Figure 8f), which was ~~barely reproduced~~ highly underestimated in the results of the  
492 CTRL run without dust. In contrast, the observed band of high IWC was reproduced by the model in DUST with much  
493 more consistent ~~location and~~ magnitude (Figure 8j).

494 At 18 UTC on April 9, 2012, the satellite was scanning the dust source over GD, which was covered by a thick dust  
495 plume between 35°N and 45°N (Figure 10a), with dust particles lifted up to 10 km above the surface (Figure 9c). High  
496 concentration of IWC was observed by the satellite at altitude from 5 km to 11 km between 30°N and 45°N (Figure  
497 9e). In this case, the model reproduced the high concentration of IWC at the observed location in the results from both  
498 CTRL and DUST, although the IWC was significantly underestimated in the results from CTRL (Figure 9g), while it  
499 was better reproduced in the results from DUST (Figure 9j).

500 Similar to the previous cases, the satellite was scanning along east coast of China at 05 UTC on April 23, 2012, when  
501 a dust plume was arriving from the dust sources and affecting areas between 35°N and 45°N (Figure 9b), and dust  
502 particles were distributed vertically from the surface to 10 km along the scanning track of the satellite (Figure 9d).

503 Along the orbit of the satellite, ~~two bands a band with of~~ high IWC ~~areas wasere~~ observed at altitudes between 5 km  
504 and 12 km, ~~one is located between 30°N and 37°N, and the other is located between 40 from 30°N to and~~ 45°N (Figure  
505 9f). In the results from CTRL, the model reproduced the ~~bands of high IWC values~~ at the correct locations, but with  
506 substantially lower values (Figure 9h); however, upon taking into account the effect of dust in the GOCART-  
507 Thompson microphysics scheme, the ~~bands of high IWC areas~~ were well reproduced by the model, with much more  
508 consistent values (Figure 9j).

509 By comparing the satellite-observational and simulated vertical profiles of IWC during the various dust events, it was  
510 demonstrated that ~~by considering the effects of dust on ice nucleation process,~~ the model reproduces the enhancement  
511 of IWC clouds in the mid- to upper troposphere by taking in to account the effect of dust in the ice nucleation process,  
512 which substantially improves the simulation of cloud ice.

513

### 514 6.2.3 Mean vertical profiles of IWC

515 The mean profiles of the observed IWC, as well as the simulated IWC from CTRL and DUST for the four dust events  
516 discussed in Section 6.2.2, are shown in Figure 10. Note that the “mean profile” of IWC is the average over the  
517 available data points for the IWC along the orbit of the satellite between 30°N to 45°N for each of the dust events  
518 shown in Figures 8 and 9.

519 Compared with the results from CTRL, the vertical profile of the simulated IWC was substantially improved in DUST  
520 for each dust event, with the enhancement of the ice nucleation process well captured by the GOCART-Thompson  
521 microphysics scheme. However, there were still discrepancies between observations and the simulation results from  
522 DUST, the magnitudes of the vertical IWC produced by the model were always lower than the observed values.

523 For the cases on March 21 and April 1, the peaks of IWC were observed at 9.5 km and 8 km, respectively, whereas  
524 the simulated peak of IWC were located at 7.8 km and 7.5 km, respectively, with lower peak values. The lower peak  
525 value for the case on March 21 was due to the missing of the high IWC observed between 30°N to 45°N in the  
526 simulation results (Figure 8e and i), while the lower peak value for the case on April 1 was due to the underestimation  
527 of the IWC around 35°N (Figure 8f and j). The locations of the peaks of simulated IWC for the cases on April 9 and  
528 April 23 were more consistent with the observed peaks, but still possessed lower values due to the missing or  
529 underestimation of high IWC with respect to the observations.

530

### 531 **6.3 Sensitivity test and discussion**

532 As discussed in Section 6.2.3, the simulation of cloud ice is greatly improved by considering the enhancement of ice  
533 nucleation process induced by dust, which is well captured by the GOCART-Thompson microphysics scheme.  
534 However, the IWC is still underestimated by the model during dust events. To determine the reason for this limitation,  
535 numerical experiments were performed to investigate the sensitivity of simulated IWC to the parameters of the ice  
536 nucleation parameterization in the GOCART-Thompson microphysics scheme.

537

#### 538 **6.3.1 Calibration factor $c_f$**

539 The calibration factor  $c_f$  is an empirical tuning coefficient derived from observational data from field and laboratory  
540 experiments. It ranges from 1 to 6, and recommended to be 3 (DeMott et al., 2015), which was applied in the previous  
541 simulations. Three other experiments were conducted to investigate the sensitivity of the simulated IWC to  $c_f$  values  
542 ranging from 3 to 6.

543 The mean profiles of IWC from simulation results were compared with the CALIPSO observations for the dust events  
544 discussed in Section 6.2.2 and 6.2.3, as shown in Figure 11. For the cases on March 21 and April 1, changing  $c_f$  did  
545 not result in an increase of IWC; instead, the simulated IWC remained consistent for  $c_f$  values varying from 3 to 6.

546 For the case on April 9, the simulated IWC increased between 6 km and 9 km and was ~~higher and closer to~~ the  
547 observed profile when  $c_f$  was equal to ~~5~~4 and ~~6~~5; ~~however, compared to the case~~ when  $c_f$  was set to 3 and ~~4~~6, ~~the~~  
548 ~~simulated IWC was lower than that obtained with  $c_f$  values of 4 or 5.~~

549 For the case on April 23, two peaks were observed in the profiles of simulated IWC, located at 7 km and 10 km. ~~By~~  
550 ~~increasing  $c_f$  values from 3 to 6,~~ the simulated IWC remained unchanged ~~with  $c_f$  values varying from 3 to 6~~ for the  
551 peak at 10 km, but ~~gradually~~ increased ~~upon changing the  $c_f$  from 3 to 4, and remained the same upon changing the~~  
552  ~~$c_f$  from 5 and 6 for for~~ the peak ~~at 7 km~~. The peak of the simulated IWC at 7 km should correspond to the observed  
553 peak between 6 km to 8 km, which was slightly overestimated by the model.

554 In summary, increasing the calibration factor  $c_f$  from 3 to 6 does not necessarily lead to a significant variation in the  
555 simulated IWC during dust events, and the model achieves a relatively better performance in reproducing the profile  
556 of IWC when the  $c_f$  is set to ~~4 or~~5.

557 As ice nucleation occurs only in a super-saturated atmosphere with respect to water vapor, the ice nucleation process  
558 would be terminated in the GOCART-Thompson microphysics scheme when the environmental  $RH_i$  is lower than the  
559 threshold  $RH_i$ , which was set to 105% for the simulations in this study. The consistency in the simulated IWC with  
560 increasing  $c_f$  for the cases in Figure 11 indicates that in these cases, the environmental  $RH_i$  had already reached below  
561 105% when  $c_f$  was set to 3, meaning that the water vapor available for freezing into ice crystals has been consumed  
562 up with  $c_f$  equal to 3, therefore, increasing  $c_f$  could not lead to a further increase in simulated IWC. Given the above,  
563 lowering the threshold  $RH_i$  might result in an enhancement of the ice nucleation process as well as the simulated IWC,  
564 which will be discussed in the following section.

565

### 566 6.3.2 Threshold of relative humidity

567 In this study, the threshold relative humidity to trigger the ice nucleation process in the simulation was originally set  
568 to 105%, which was selected for the central lamina condition in the laboratory experiments to derive the DeMott2015  
569 ice nucleation scheme (DeMott et al., 2015). However, as reported in other studies, the number of ice nucleating  
570 particles starts to rise when the relative humidity exceeds 100% (DeMott et al., 2011). Therefore, a sensitivity  
571 experiment was carried out to investigate the response of simulated IWC to lower threshold relative humidity.

572 The mean profiles of IWC from the simulation results were compared with the CALIPSO observations for the  
573 aforementioned dust events, as shown in Figure 12. With the threshold relative humidity lowered to 100%, the  
574 simulated IWC showed an increase throughout the vertical profile with the most significant increase at the peaks,  
575 suggesting more consistency with the observations for all of the dust events, except the one on April 1. In the case on  
576 April 1, the simulated IWC increased at lower altitudes than the observed peak, but slightly decreased right at the peak  
577 with lowering the threshold relative humidity to 100%. Overall, the simulation of IWC during dust events was  
578 significantly improved by lowering the threshold relative humidity from 105% to 100%.

579

## 580 **7 Conclusions**

581 A new treatment, the GOCART–Thompson scheme, was implemented into WRF-Chem to couple the GOCART  
582 aerosol model to the aerosol-aware Thompson-Eidhammer microphysics scheme. By applying this newly-  
583 implemented microphysics scheme, the effect of dust on the ice nucleation process by serving as IN in the atmosphere  
584 can be quantified and evaluated. Numerical experiments, including a control run without dust and a test run with dust,  
585 were then carried out to evaluate the performance of the newly–implemented GOCART–Thompson microphysics  
586 scheme in simulating the effect of dust on the content of cloud ice over East Asia during a typical dust-intensive period,  
587 by comparing the simulation results with various observations.

588 Based on the GOCART aerosol model the model reproduced dust emission reasonably well, by capturing the evolution  
589 and magnitude of surface PM<sub>10</sub> concentration at the locations of various environmental monitoring stations and the  
590 AOD at two AERONET sites. The spatial patterns of the mean AOD over East Asia during the simulation period were  
591 also consistent with satellite observations.

592 The effect of dust on the ice nucleation process was then quantified and evaluated in the GOCART–Thompson  
593 microphysics scheme. Upon considering the effect of dust in the simulation, the simulated ice water mixing ratio and  
594 ice crystal number concentration over East Asia were ~~one order of magnitude~~ 15% and 7% higher than those simulated  
595 without dust, with the most significant enhancements located over dust source regions and downwind areas.

596 Comparison between the vertical profiles of the satellite-observed and simulated IWC during various dust events  
597 indicated that the enhancement of cloud ice induced by abundant dust particles serving as IN is well captured by the  
598 GOCART–Thompson microphysics scheme, with the results from the simulation with dust much more consistent with  
599 the satellite–observations, although the IWC is generally underestimated by the model.

600 Sensitivity experiments revealed that the simulated IWC was not very sensitive to the calibration factor defined in the  
601 DeMott2015 ice nucleation scheme, but the model delivered a slight better performance in reproducing the IWC when  
602 the calibration factor was set to ~~3~~ ~~or~~ 4.5. However, the simulated IWC was sensitive to the threshold relative humidity  
603 to trigger the ice nucleation process in the model and was improved upon lowering the threshold relative humidity  
604 from 105% to 100%.

605

606 **Acknowledgement.** We would like to acknowledge the provision of the MODIS and the MISR observations by the  
607 Ministry of Environmental Protection Data Center, U.S. National Center for Atmospheric Research (NCAR), and the  
608 CALIPSO data by the U.S. National Aeronautics and Space Administration (NASA) Data Center. We thank the  
609 principal investigators and their staff for establishing and maintaining the two AERONET sites used in this study. The  
610 AERONET data were obtained freely from the AERONET program website (<https://aeronet.gsfc.nasa.gov/>). We  
611 appreciate the assistance of the Hong Kong Observatory (HKO), which provided the meteorological data. Lin Su  
612 would like to thank Dr. Georg Grell, Dr. Stuart McKeen, and Dr. Ravan Ahmandov from the Earth System Research  
613 Laboratory, U.S. National Oceanic and Atmospheric Administration for insightful discussions. Other data used this  
614 paper are properly cited and referred to in the reference list. All data shown in the results are available upon request.

615 This work was supported by NSFC/RGC Grant N\_HKUST631/05,  
616 NSFC-FD Grant U1033001, and the RGC Grant 16303416.

617

618 **References**

- 619 Atkinson, J. D., Murray, B. J., Woodhouse, M. T., Whale, T. F., Baustian, K. J., Carslaw, K. S., Dobbie, S.,  
620 O'sullivan, D., and Malkin, T. L.: The importance of feldspar for ice nucleation by mineral dust in mixed-  
621 phase clouds, *Nature*, 498, 355, 2013.
- 622 Baró, R., Jiménez-Guerrero, P., Balzarini, A., Curci, G., Forkel, R., Grell, G., Hirtl, M., Honzak, L., Langer,  
623 M., and Pérez, J. L.: Sensitivity analysis of the microphysics scheme in WRF-Chem contributions to  
624 AQMEII phase 2, *Atmospheric Environment*, 115, 620-629, 2015.
- 625 Bi, J., Huang, J., Fu, Q., Ge, J., Shi, J., Zhou, T., and Zhang, W.: Field measurement of clear-sky solar  
626 irradiance in Badain Jaran Desert of Northwestern China, *Journal of Quantitative Spectroscopy and  
627 Radiative Transfer*, 122, 194-207, 2013.
- 628 Chapman, E. G., Gustafson Jr, W., Easter, R. C., Barnard, J. C., Ghan, S. J., Pekour, M. S., and Fast, J. D.:  
629 Coupling aerosol-cloud-radiative processes in the WRF-Chem model: Investigating the radiative impact of  
630 elevated point sources, *Atmospheric Chemistry and Physics*, 9, 945-964, 2009.
- 631 Chin, M., Rood, R. B., Lin, S.-J., Müller, J.-F., and Thompson, A. M.: Atmospheric sulfur cycle simulated  
632 in the global model GOCART: Model description and global properties, 2000.
- 633 DeMott, P. J., Sassen, K., Poellot, M. R., Baumgardner, D., Rogers, D. C., Brooks, S. D., Prenni, A. J., and  
634 Kreidenweis, S. M.: African dust aerosols as atmospheric ice nuclei, *Geophysical Research Letters*, 30,  
635 2003.
- 636 DeMott, P. J., Prenni, A. J., Liu, X., Kreidenweis, S. M., Petters, M. D., Twohy, C. H., Richardson, M.,  
637 Eidhammer, T., and Rogers, D.: Predicting global atmospheric ice nuclei distributions and their impacts on  
638 climate, *Proceedings of the National Academy of Sciences*, 107, 11217-11222, 2010.
- 639 DeMott, P. J., Möhler, O., Stetzer, O., Vali, G., Levin, Z., Petters, M. D., Murakami, M., Leisner, T.,  
640 Bundke, U., and Klein, H.: Resurgence in ice nuclei measurement research, *Bulletin of the American  
641 Meteorological Society*, 92, 1623-1635, 2011.
- 642 DeMott, P. J., Prenni, A. J., McMeeking, G. R., Sullivan, R. C., Petters, M. D., Tobo, Y., Niemand, M.,  
643 Möhler, O., Snider, J. R., and Wang, Z.: Integrating laboratory and field data to quantify the immersion  
644 freezing ice nucleation activity of mineral dust particles, *Atmospheric Chemistry and Physics*, 15, 393-409,  
645 2015.
- 646 Diner, D. J., Barge, L. M., Bruegge, C. J., Chrien, T. G., Conel, J. E., Eastwood, M. L., Garcia, J. D.,  
647 Hernandez, M. A., Kurzweil, C. G., and Ledebor, W. C.: The Airborne Multi-angle Imaging  
648 SpectroRadiometer (AirMISR): instrument description and first results, *IEEE Transactions on Geoscience  
649 and Remote Sensing*, 36, 1339-1349, 1998.

Formatted: Line spacing: 1.5 lines

Formatted: Font: (Default) Times New Roman, 11 pt



650 Duce, R., Liss, P., Merrill, J., Atlas, E., Buat-Menard, P., Hicks, B., Miller, J., Prospero, J., Arimoto, R.,  
651 and Church, T.: The atmospheric input of trace species to the world ocean, *Global biogeochemical cycles*,  
652 5, 193-259, 1991.

653 Ge, J., Su, J., Ackerman, T., Fu, Q., Huang, J., and Shi, J.: Dust aerosol optical properties retrieval and  
654 radiative forcing over northwestern China during the 2008 China-US joint field experiment, *Journal of*  
655 *Geophysical Research: Atmospheres*, 115, 2010.

656 Ginoux, P., Chin, M., Tegen, I., Prospero, J. M., Holben, B., Dubovik, O., and Lin, S. J.: Sources and  
657 distributions of dust aerosols simulated with the GOCART model, *Journal of Geophysical Research:*  
658 *Atmospheres*, 106, 20255-20273, 2001.

659 Ginoux, P., Prospero, J. M., Torres, O., and Chin, M.: Long-term simulation of global dust distribution with  
660 the GOCART model: correlation with North Atlantic Oscillation, *Environmental Modelling & Software*,  
661 19, 113-128, 2004.

662 Grell, G., Peckham, S., Fast, J., Singh, B., Easter, R., Gustafson, W., Rasch, P., Wolters, S., Barth, M., and  
663 Pfister, G.: WRF-Chem V3. 5: A summary of status and updates, *EGU General Assembly Conference*  
664 *Abstracts*, 2013, 11332.

665 Grell, G. A., and Freitas, S. R.: A scale and aerosol aware stochastic convective parameterization for  
666 weather and air quality modeling, *Atmos. Chem. Phys*, 14, 5233-5250, 2014.

667 Hansen, J., Sato, M., and Ruedy, R.: Radiative forcing and climate response, *Journal of Geophysical*  
668 *Research: Atmospheres*, 102, 6831-6864, 1997.

669 Hartmann, D., Tank, A., and Rusticucci, M.: IPCC fifth assessment report, climate change 2013: The  
670 physical science basis, *IPCC AR5*, 31-39, 2013.

671 Holben, B., Tanre, D., Smirnov, A., Eck, T., Slutsker, I., Abuhassan, N., Newcomb, W., Schafer, J.,  
672 Chatenet, B., and Lavenu, F.: An emerging ground-based aerosol climatology: Aerosol optical depth from  
673 AERONET, *Journal of Geophysical Research: Atmospheres*, 106, 12067-12097, 2001.

674 Hoose, C., Lohmann, U., Erdin, R., and Tegen, I.: The global influence of dust mineralogical composition  
675 on heterogeneous ice nucleation in mixed-phase clouds, *Environmental Research Letters*, 3, 025003, 2008.

676 Horvath, H.: Influence of atmospheric aerosols upon the global radiation balance, *Atmospheric particles*, 5,  
677 62-63, 1998.

678 Hsu, N. C., Tsay, S.-C., King, M. D., and Herman, J. R.: Deep blue retrievals of Asian aerosol properties  
679 during ACE-Asia, *IEEE Transactions on Geoscience and Remote Sensing*, 44, 3180-3195, 2006.

680 Hsu, S. C., Liu, S. C., Arimoto, R., Liu, T. H., Huang, Y. T., Tsai, F., Lin, F. J., and Kao, S. J.: Dust  
681 deposition to the East China Sea and its biogeochemical implications, *Journal of Geophysical Research:*  
682 *Atmospheres*, 114, 2009.

Formatted: Font: (Default) Times New Roman, 11 pt

Formatted: Font: (Default) Cambria Math, 11 pt

Formatted: Font: (Default) Times New Roman, 11 pt

Formatted: Font: (Default) Times New Roman, 11 pt

683 Huang, J., Fu, Q., Su, J., Tang, Q., Minnis, P., Hu, Y., Yi, Y., and Zhao, Q.: Taklimakan dust aerosol  
684 radiative heating derived from CALIPSO observations using the Fu-Liou radiation model with CERES  
685 constraints, *Atmospheric Chemistry and Physics*, 9, 4011-4021, 2009.

686 Huang, J.: Emission, transport, and radiative effects of mineral dust from the Taklimakan and Gobi deserts:  
687 comparison of measurements and model results, *Atmos. Chem. Phys.*, 1680, 7324, 2017.

688 Iacono, M. J., Delamere, J. S., Mlawer, E. J., Shephard, M. W., Clough, S. A., and Collins, W. D.: Radiative  
689 forcing by long-lived greenhouse gases: Calculations with the AER radiative transfer models, *Journal of*  
690 *Geophysical Research: Atmospheres*, 113, 2008.

691 Janjić, Z. I.: The step-mountain eta coordinate model: Further developments of the convection, viscous  
692 sublayer, and turbulence closure schemes, *Monthly Weather Review*, 122, 927-945, 1994.

693 Janjić, Z. I.: Nonsingular implementation of the Mellor–Yamada level 2.5 scheme in the NCEP Meso model,  
694 NCEP office note, 437, 61, 2002.

695 Kang, J. Y., Yoon, S. C., Shao, Y., and Kim, S. W.: Comparison of vertical dust flux by implementing three  
696 dust emission schemes in WRF/Chem, *Journal of Geophysical Research: Atmospheres*, 116, 2011.

697 Karydis, V., Kumar, P., Barahona, D., Sokolik, I., and Nenes, A.: On the effect of dust particles on global  
698 cloud condensation nuclei and cloud droplet number, *Journal of Geophysical Research: Atmospheres*, 116,  
699 2011.

700 Kaufman, Y., Tanré, D., Remer, L. A., Vermote, E., Chu, A., and Holben, B.: Operational remote sensing  
701 of tropospheric aerosol over land from EOS moderate resolution imaging spectroradiometer, *Journal of*  
702 *Geophysical Research: Atmospheres*, 102, 17051-17067, 1997.

703 Koehler, K., Kreidenweis, S., DeMott, P., Petters, M., Prenni, A., and Möhler, O.: Laboratory investigations  
704 of the impact of mineral dust aerosol on cold cloud formation, *Atmospheric Chemistry and Physics*, 10,  
705 11955-11968, 2010.

706 Koop, T., Luo, B., Tsias, A., and Peter, T.: Water activity as the determinant for homogeneous ice  
707 nucleation in aqueous solutions, *Nature*, 406, 611-614, 2000.

708 Lacis, A.: Climate forcing, climate sensitivity, and climate response: A radiative modeling perspective on  
709 atmospheric aerosols, *Aerosol forcing of climate*, 11-42, 1995.

710 Liu, Huang, J., Shi, G., Takamura, T., Khatri, P., Bi, J., Shi, J., Wang, T., Wang, X., and Zhang, B.: Aerosol  
711 optical properties and radiative effect determined from sky-radiometer over Loess Plateau of Northwest  
712 China, *Atmospheric Chemistry and Physics*, 11, 11455-11463, 2011a.

713 Liu, Zheng, Y., Li, Z., Flynn, C., Welton, E. J., and Cribb, M.: Transport, vertical structure and radiative  
714 properties of dust events in southeast China determined from ground and space sensors, *Atmospheric*  
715 *environment*, 45, 6469-6480, 2011b.

Formatted: Font: (Default) Times New Roman, 11 pt

716 Lohmann, U., and Diehl, K.: Sensitivity studies of the importance of dust ice nuclei for the indirect aerosol  
717 effect on stratiform mixed-phase clouds, *Journal of the Atmospheric Sciences*, 63, 968-982, 2006.

718 Mallet, M., Tulet, P., Serça, D., Solmon, F., Dubovik, O., Pelon, J., Pont, V., and Thouron, O.: Impact of  
719 dust aerosols on the radiative budget, surface heat fluxes, heating rate profiles and convective activity over  
720 West Africa during March 2006, *Atmospheric Chemistry and Physics*, 9, 7143-7160, 2009.

721 Martonchik, J., Diner, D., Kahn, R., Gaitley, B., and Holben, B.: Comparison of MISR and AERONET  
722 aerosol optical depths over desert sites, *Geophysical Research Letters*, 31, 2004.

723 Miller, R., Tegen, I., and Perlwitz, J.: Surface radiative forcing by soil dust aerosols and the hydrologic  
724 cycle, *Journal of Geophysical Research: Atmospheres*, 109, 2004.

725 Mlawer, E. J., Taubman, S. J., Brown, P. D., Iacono, M. J., and Clough, S. A.: Radiative transfer for  
726 inhomogeneous atmospheres: RRTM, a validated correlated-k model for the longwave, *Journal of*  
727 *Geophysical Research: Atmospheres*, 102, 16663-16682, 1997.

728 Nabat, P., Somot, S., Mallet, M., Michou, M., Sevault, F., Driouech, F., Meloni, D., Di Sarra, A., Di Biagio,  
729 C., and Formenti, P.: Dust aerosol radiative effects during summer 2012 simulated with a coupled regional  
730 aerosol-atmosphere-ocean model over the Mediterranean, *Atmospheric Chemistry and Physics*, 15, 3303-  
731 3326, 2015a.

732 Nabat, P., Somot, S., Mallet, M., Sevault, F., Chiacchio, M., and Wild, M.: Direct and semi-direct aerosol  
733 radiative effect on the Mediterranean climate variability using a coupled regional climate system model,  
734 *Climate dynamics*, 44, 1127-1155, 2015b.

735 Perlwitz, J., and Miller, R. L.: Cloud cover increase with increasing aerosol absorptivity: A counterexample  
736 to the conventional semidirect aerosol effect, *Journal of Geophysical Research: Atmospheres*, 115, 2010.

737 Phillips, V. T., DeMott, P. J., and Andronache, C.: An empirical parameterization of heterogeneous ice  
738 nucleation for multiple chemical species of aerosol, *Journal of the atmospheric sciences*, 65, 2757-2783,  
739 2008.

740 Seigel, R., Van Den Heever, S., and Saleeby, S.: Mineral dust indirect effects and cloud radiative feedbacks  
741 of a simulated idealized nocturnal squall line, *Atmospheric Chemistry and Physics*, 13, 4467-4485, 2013.

742 Shao: A model for mineral dust emission, *Journal of Geophysical Research: Atmospheres*, 106, 20239-  
743 20254, 2001.

744 Shao: Simplification of a dust emission scheme and comparison with data, *Journal of Geophysical Research:*  
745 *Atmospheres*, 109, 2004.

746 Shao, Ishizuka, M., Mikami, M., and Leys, J.: Parameterization of size-resolved dust emission and  
747 validation with measurements, *Journal of Geophysical Research: Atmospheres*, 116, 2011.

748 Soil Survey Staff: Soil survey manual, 1993.

Formatted: Font: (Default) Times New Roman, 11 pt

Formatted: Font: (Default) Times New Roman, 11 pt

Formatted: Font: (Default) Cambria Math, 11 pt

Formatted: Font: (Default) Times New Roman, 11 pt

749 Solomos, S., Kallos, G., Kushta, J., Astitha, M., Tremback, C., Nenes, A., and Levin, Z.: An integrated  
750 modeling study on the effects of mineral dust and sea salt particles on clouds and precipitation, *Atmospheric*  
751 *Chemistry and Physics*, 11, 873-892, 2011.

752 Su, L., and Fung, J. C.: Sensitivities of WRF-Chem to dust emission schemes and land surface properties  
753 in simulating dust cycles during springtime over East Asia, *Journal of Geophysical Research: Atmospheres*,  
754 120, 2015.

755 Tesfaye, M., Tsidu, G. M., Botai, J., and Sivakumar, V.: Mineral dust aerosol distributions, its direct and  
756 semi-direct effects over South Africa based on regional climate model simulation, *Journal of Arid*  
757 *Environments*, 114, 22-40, 2015.

758 Textor, C., Schulz, M., Guibert, S., Kinne, S., Balkanski, Y., Bauer, S., Bernsten, T., Berglen, T., Boucher,  
759 O., and Chin, M.: Analysis and quantification of the diversities of aerosol life cycles within AeroCom,  
760 *Atmospheric Chemistry and Physics*, 6, 1777-1813, 2006.

761 Thompson, G., Rasmussen, R. M., and Manning, K.: Explicit forecasts of winter precipitation using an  
762 improved bulk microphysics scheme. Part I: Description and sensitivity analysis, *Monthly Weather Review*,  
763 132, 519-542, 2004.

764 Thompson, G., and Eidhammer, T.: A study of aerosol impacts on clouds and precipitation development in  
765 a large winter cyclone, *Journal of the Atmospheric Sciences*, 71, 3636-3658, 2014.

766 Tomasi, C., Fuzzi, S., and Kokhanovsky, A.: *Atmospheric Aerosols: Life Cycles and Effects on Air Quality*  
767 *and Climate*, John Wiley & Sons, 2017.

768 Twohy, C. H., Kreidenweis, S. M., Eidhammer, T., Browell, E. V., Heymsfield, A. J., Bansemer, A. R.,  
769 Anderson, B. E., Chen, G., Ismail, S., and DeMott, P. J.: Saharan dust particles nucleate droplets in eastern  
770 Atlantic clouds, *Geophysical Research Letters*, 36, 2009.

771 Vaughan, M. A., Young, S. A., Winker, D. M., Powell, K. A., Omar, A. H., Liu, Z., Hu, Y., and Hostetler,  
772 C. A.: Fully automated analysis of space-based lidar data: An overview of the CALIPSO retrieval  
773 algorithms and data products, *Remote Sensing*, 2004, 16-30.

774 Wesely, M.: Parameterization of surface resistances to gaseous dry deposition in regional-scale numerical  
775 models, *Atmospheric Environment (1967)*, 23, 1293-1304, 1989.

776 Winker, Pelon, J., Coakley Jr, J., Ackerman, S., Charlson, R., Colarco, P., Flamant, P., Fu, Q., Hoff, R.,  
777 and Kittaka, C.: The CALIPSO mission: A global 3D view of aerosols and clouds, *Bulletin of the American*  
778 *Meteorological Society*, 91, 1211-1229, 2010.

779 Winker, D. M., Vaughan, M. A., Omar, A., Hu, Y., Powell, K. A., Liu, Z., Hunt, W. H., and Young, S. A.:  
780 Overview of the CALIPSO mission and CALIOP data processing algorithms, *Journal of Atmospheric and*  
781 *Oceanic Technology*, 26, 2310-2323, 2009.

Formatted: Font: (Default) Times New Roman, 11 pt

Formatted: Font: (Default) Cambria Math, 11 pt

Formatted: Font: (Default) Times New Roman, 11 pt

782 Zhang, C., Wang, M., Morrison, H., Somerville, R. C., Zhang, K., Liu, X., and Li, J. L. F.: Investigating  
783 ice nucleation in cirrus clouds with an aerosol-enabled Multiscale Modeling Framework, Journal of  
784 Advances in Modeling Earth Systems, 6, 998-1015, 2014.

785

786

**Formatted:** Font: (Default) Times New Roman, 11 pt

787 **List of tables and figures**

788 Table 1: Performance statistics for the model in simulating surface  $PM_{10}$  concentrations at environmental monitoring  
789 stations during the simulation period.

790 Figure 1: Nested domain set for the simulations. Blue dots represent the ten monitoring stations used for model  
791 validation. TD: the Taklimakan Desert; GD: The Gobi Desert.

792 Figure 2: Time series of spatially averaged daily dust mass load (a) and daily number density of dust particles (b) over  
793 East Asia (domain 1) during the simulation period.

794 Figure 3: Time series of hourly observed and simulated surface  $PM_{10}$  concentrations at various environmental  
795 monitoring stations.  $r$  represents the correlation coefficient between simulation results and observations.

796 Figure 4: Time series of daily mean observed and simulated aerosol optical depths at Dalanzadgad (a) and SACOL  
797 (b).  $r$  represents the correlation coefficient between simulation results and observations.

798 Figure 5: Spatial distributions of monthly mean AOD from MODIS observations (a, b), MISR observations (c, d), and  
799 simulation results (e, f) for March (left panel) and April (right panel) of 2012.

800 Figure 6: Simulated cloud ice mixing ratio (a) and cloud ice crystal number concentration (b) at each data point from  
801 CTRL and DUST.

802 Figure 7: Spatial distributions for the temporal mean simulated cloud ice water path (a-c) and ice crystal number  
803 density (d-f) from CTRL (left panel), DUST (middle panel), and the difference between CTRL and DUST (right panel)  
804 over East Asia (domain 1) during the simulation period.

805 Figure 8: Spatial distribution for simulated dust load and satellite scanning track (a, b); the simulated vertical profile  
806 of ice-friendly aerosol (GNIFA) number concentration (c, d), with the orography represented by the shaded area; the  
807 CALIPSO vertical profile of IWC (e, f); and the simulated vertical profile of IWC from CTRL (g, h) and DUST (i, j)  
808 for the case on March 21 (left panel) and April 1 (right panel) of 2012.

809 Figure 9: As Figure 8 but for the cases on April 9 (left panel) and April 23, (right panel) of 2012.

810 Figure 10: Vertical profiles for the mean observed IWC from CALIPSO, and the simulated IWC from CTRL and  
811 DUST for dust events on March 21, April 1, April 9, and April 23, 2012.

812 Figure 11: Vertical profiles for the mean observed IWC from CALIPSO, and the simulated IWC with various  $c_f$  for  
813 the dust events on March 21, April 1, April 9, and April 23, 2012.

814 Figure 12: Vertical profiles for the mean observational IWC from CALIPSO, and the simulated IWC with threshold  
815 RH values of 105% and 100% for the dust events on March 21, April 1, April 9, and April 23, 2012.

**Table 1:** Performance statistics for the model in simulating surface PM<sub>10</sub> concentrations at environmental monitoring stations during the simulation period.

City	STATION NO.	MB (µg/m <sup>3</sup> )	ME (µg/m <sup>3</sup> )	RMSE (µg/m <sup>3</sup> )	r
BAOTOU	XCNAQ77	-36.18	80.43	94.88	0.59
	XCNAQ79	-10.05	75.83	106.58	0.62
SHIZUISHAN	XCNAQ346	72.46	121.18	317.73	0.79
	XCNAQ347	17.64	147.95	294.71	0.75
JINCHANG	XCNAQ340	-108.73	109.09	128.56	0.77
	XCNAQ342	-18.65	46.07	64.78	0.70
YAN'AN	XCNAQ335	-38.93	99.05	149.44	0.68
	XCNAQ336	-60.15	124.74	166.89	0.60
YINCHUAN	XCNAQ344	33.97	112.26	240.27	0.87
	CN_1487	-39.62	155.83	249.00	0.62
<b>Average</b>		-18.84	107.24	181.28	0.70

MB: mean bias; ME: mean error; RMSE: root mean squared error; r: correlation coefficient.



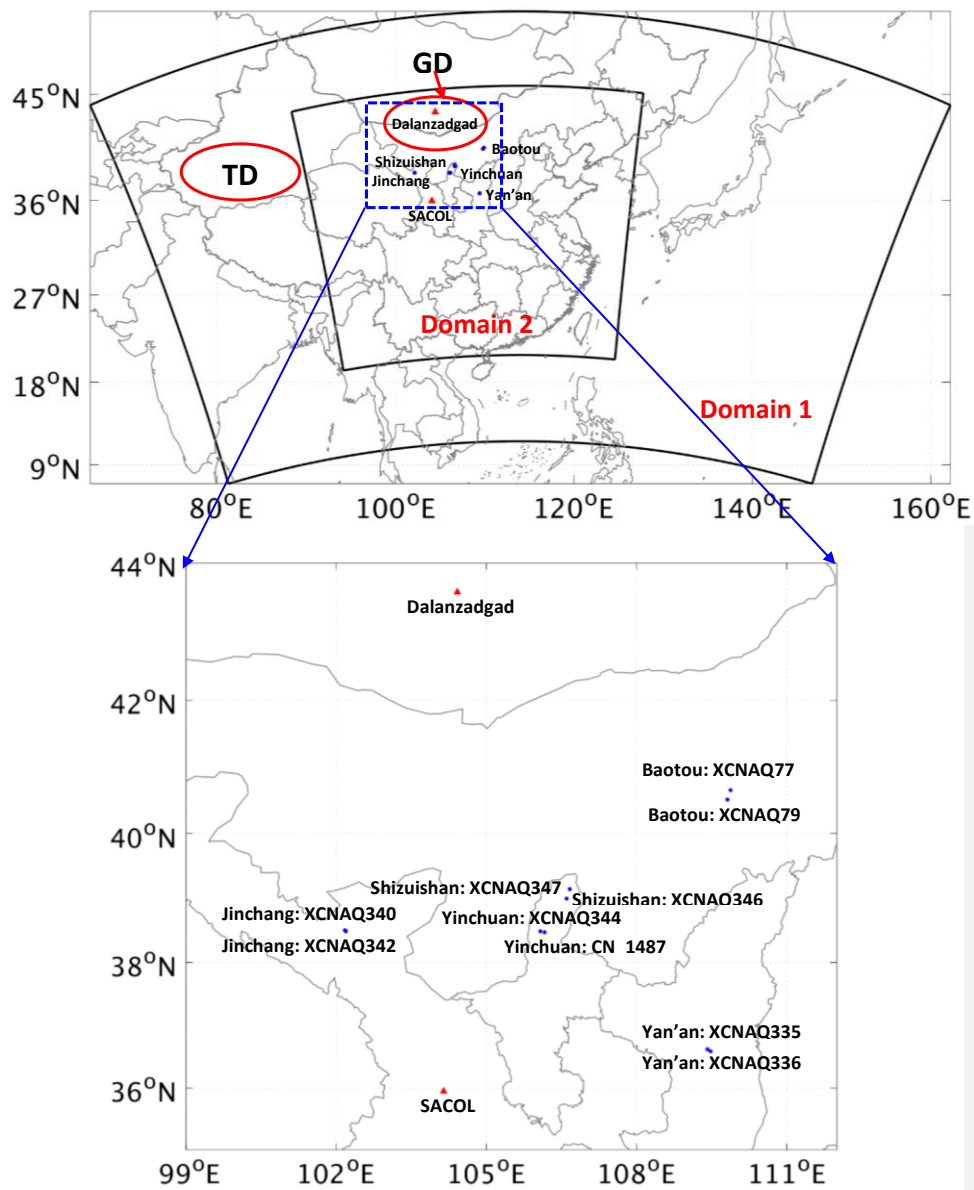


**Figure 1:** Nested domain set for the simulations. Blue dots represent the ten monitoring stations used for model validation. TD: the Taklimakan Desert; GD: The Gobi Desert.

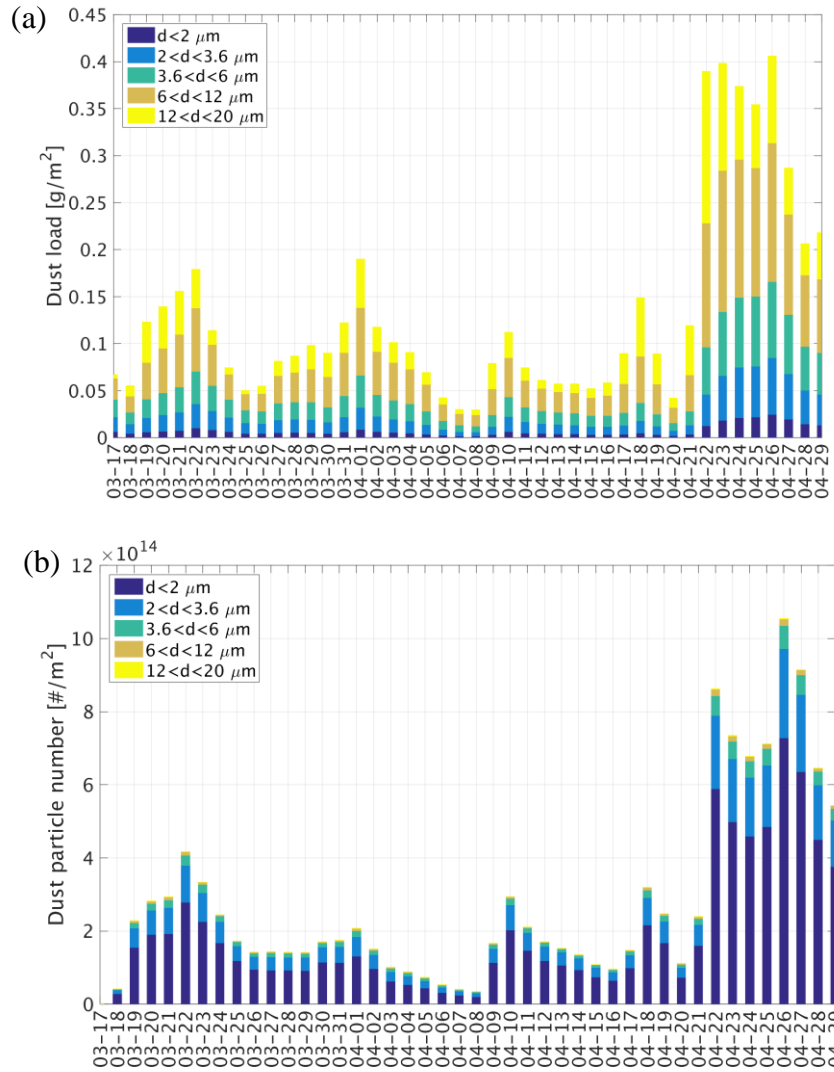


**Figure 2:** Time series of spatially averaged daily dust mass load (a) and daily number density of dust particles (b) over East Asia (domain 1) during the simulation period.

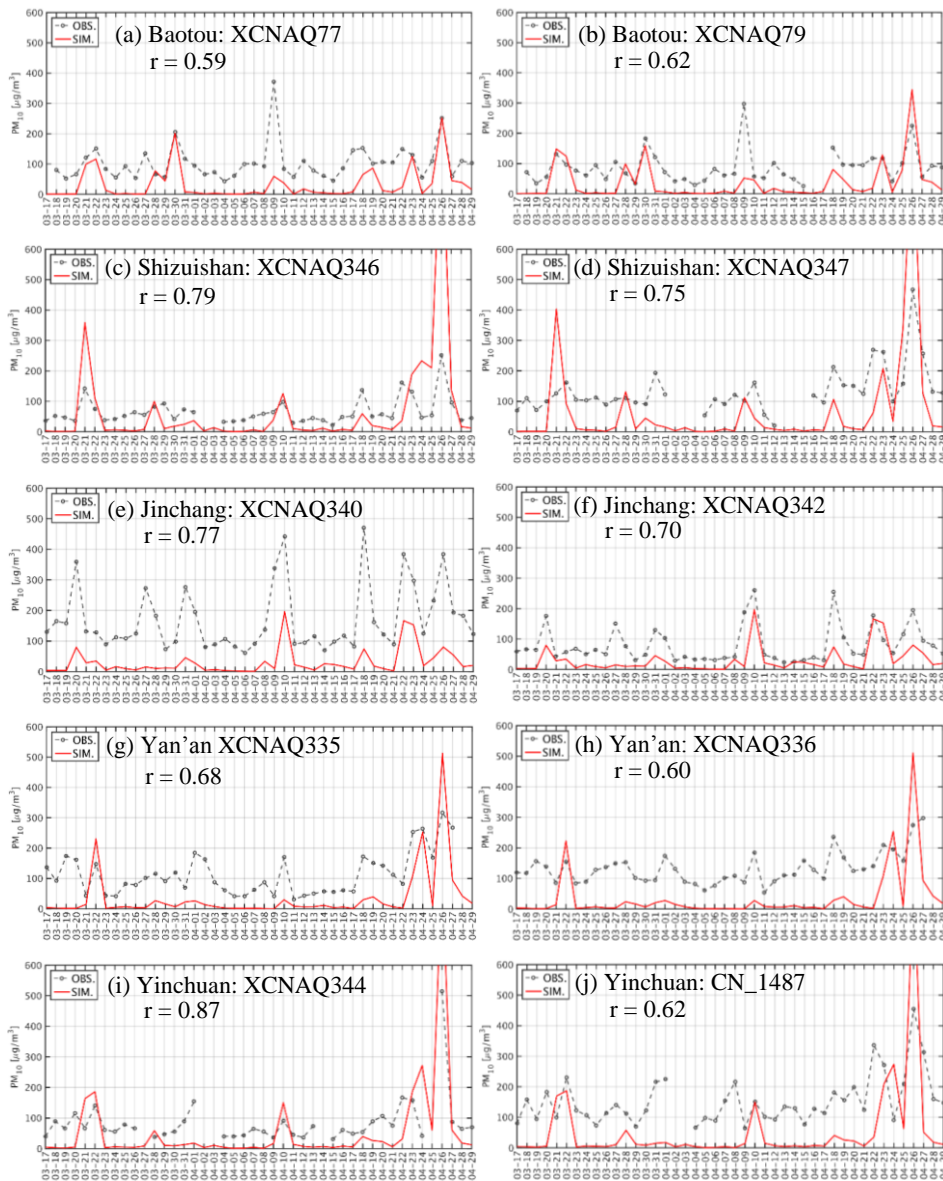


**Figure 3:** Time series of hourly observed and simulated surface  $PM_{10}$  concentrations at various environmental monitoring stations.  $r$  represents the correlation coefficient between simulation results and observations.

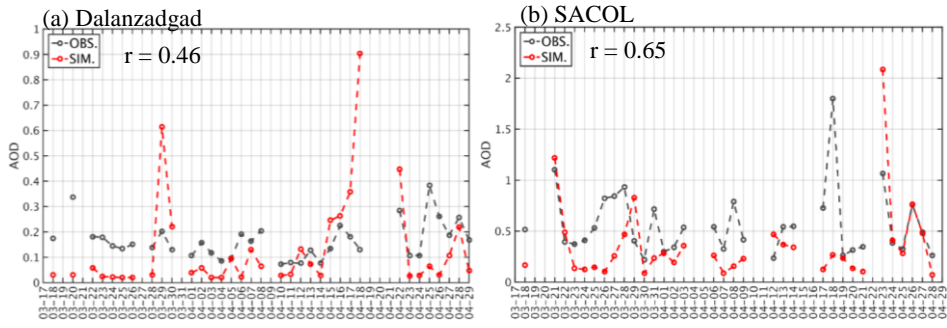


**Figure 4:** Time series of daily mean observed and simulated aerosol optical depths at Dalanzadgad (a) and SACOL (b).  $r$  represents the correlation coefficient between simulation results and observations.

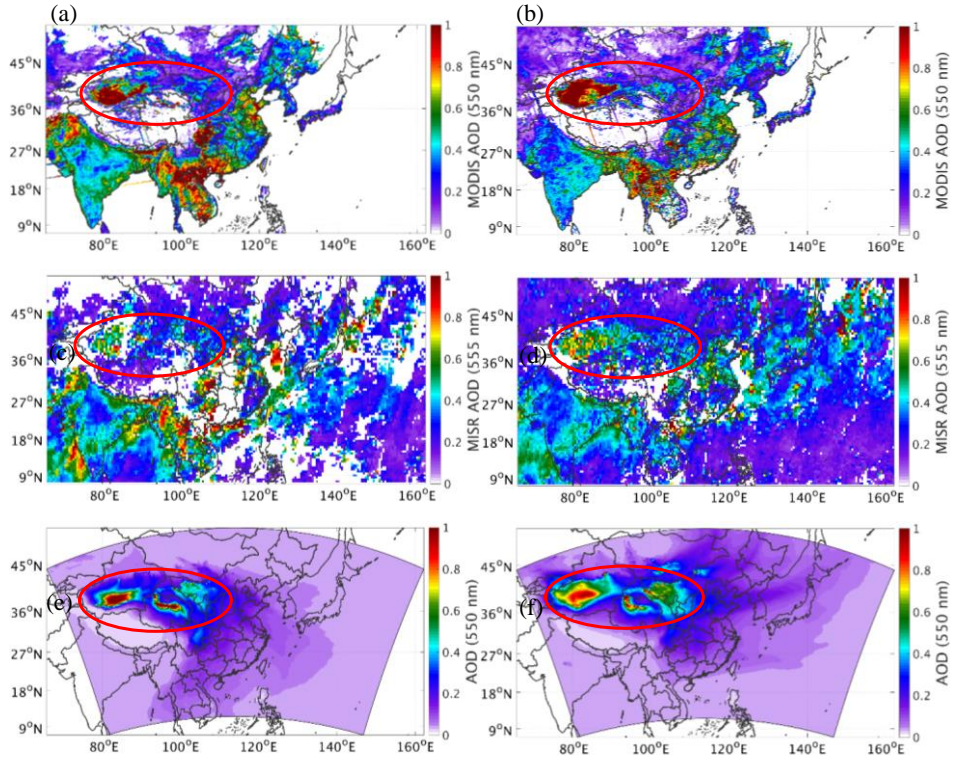


**Figure 5:** Spatial distributions of monthly mean AOD from MODIS observations (a, b), MISR observations (c, d), and simulation results (e, f) for March (left panel) and April (right panel) of 2012.

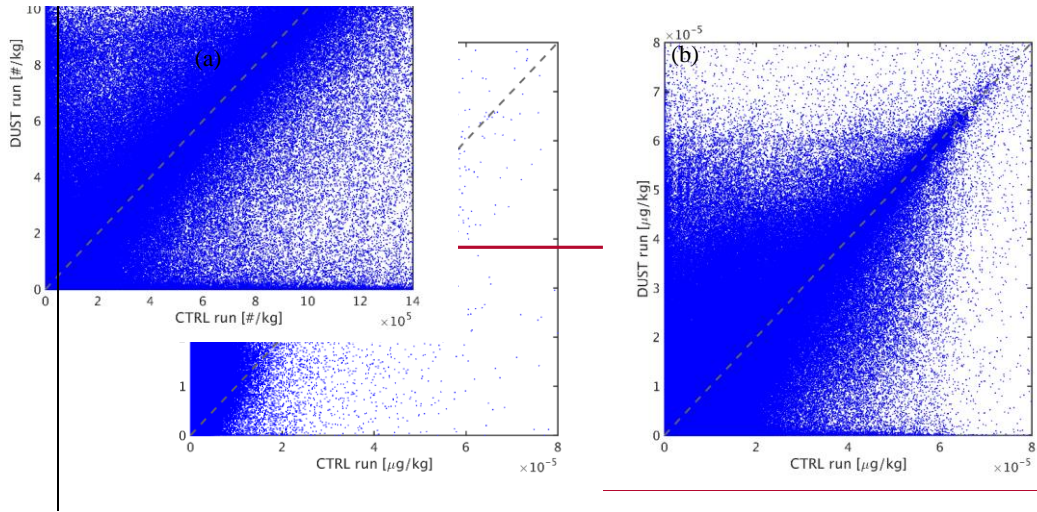


**Figure 6:** Simulated cloud ice mixing ratio (a) and cloud ice crystal number concentration (b) at each data point from CTRL and DUST.

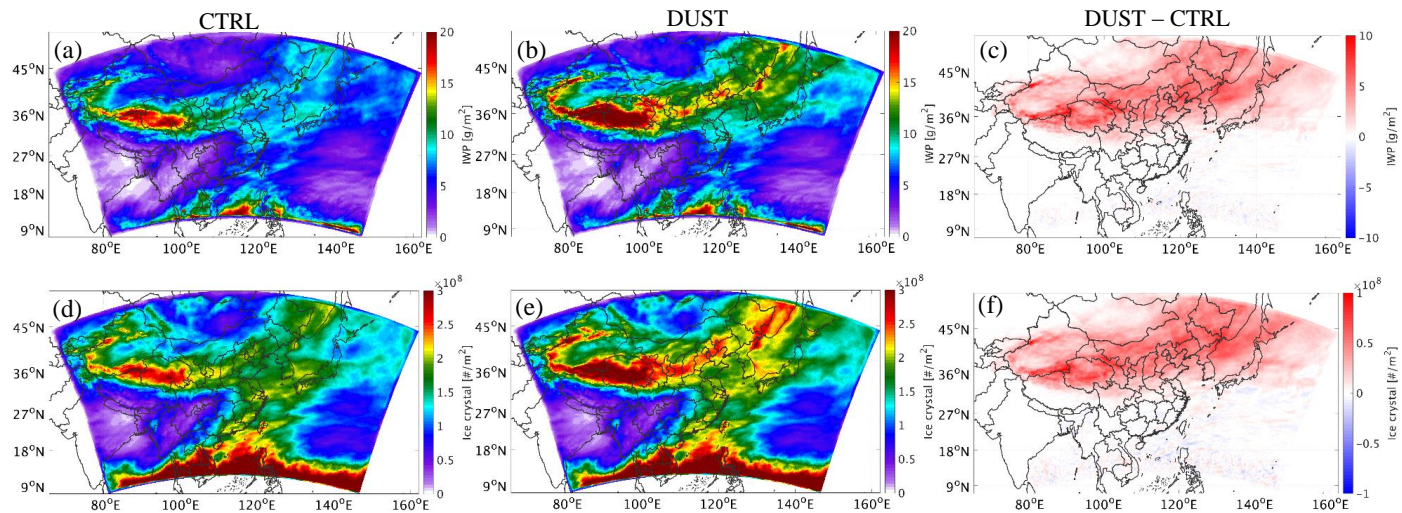


**Figure 7:** Spatial distributions for the temporal mean simulated cloud ice water path (a-c) and ice crystal number density (d-f) from CTRL (left panel), DUST (middle panel), and the difference between CTRL and DUST (right panel) over East Asia (domain 1) during the simulation period.

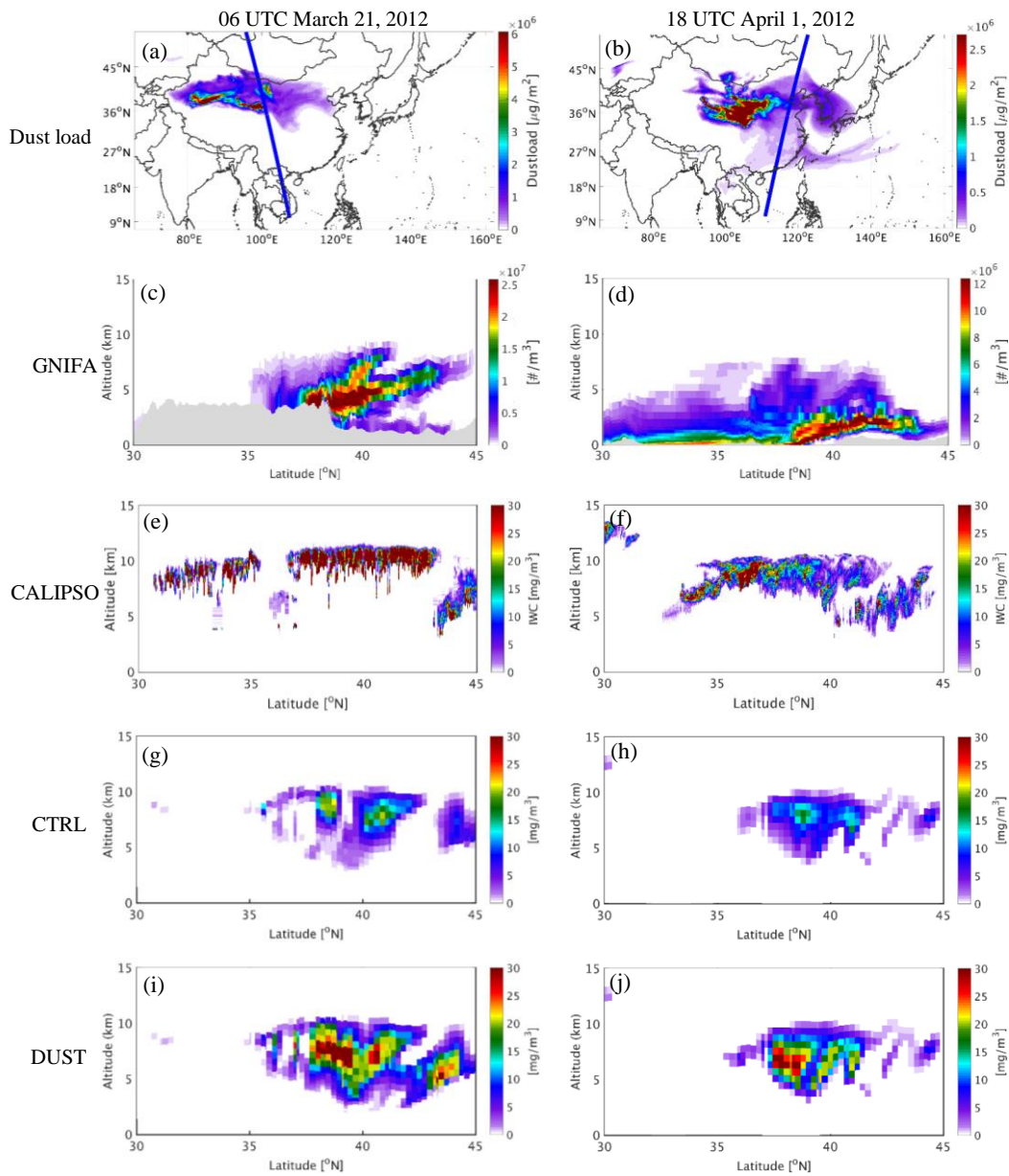


**Figure 8:** Spatial distribution for simulated dust load and satellite scanning track (a, b); the simulated vertical profile of ice-friendly aerosol (GNIFA) number concentration (c, d), with the orography represented by the shaded area; the CALIPSO vertical profile of IWC (e, f); and the simulated vertical profile of IWC from CTRL (g, h) and DUST (i, j) for the case on March 21 (left panel) and April 1 (right panel) of 2012.



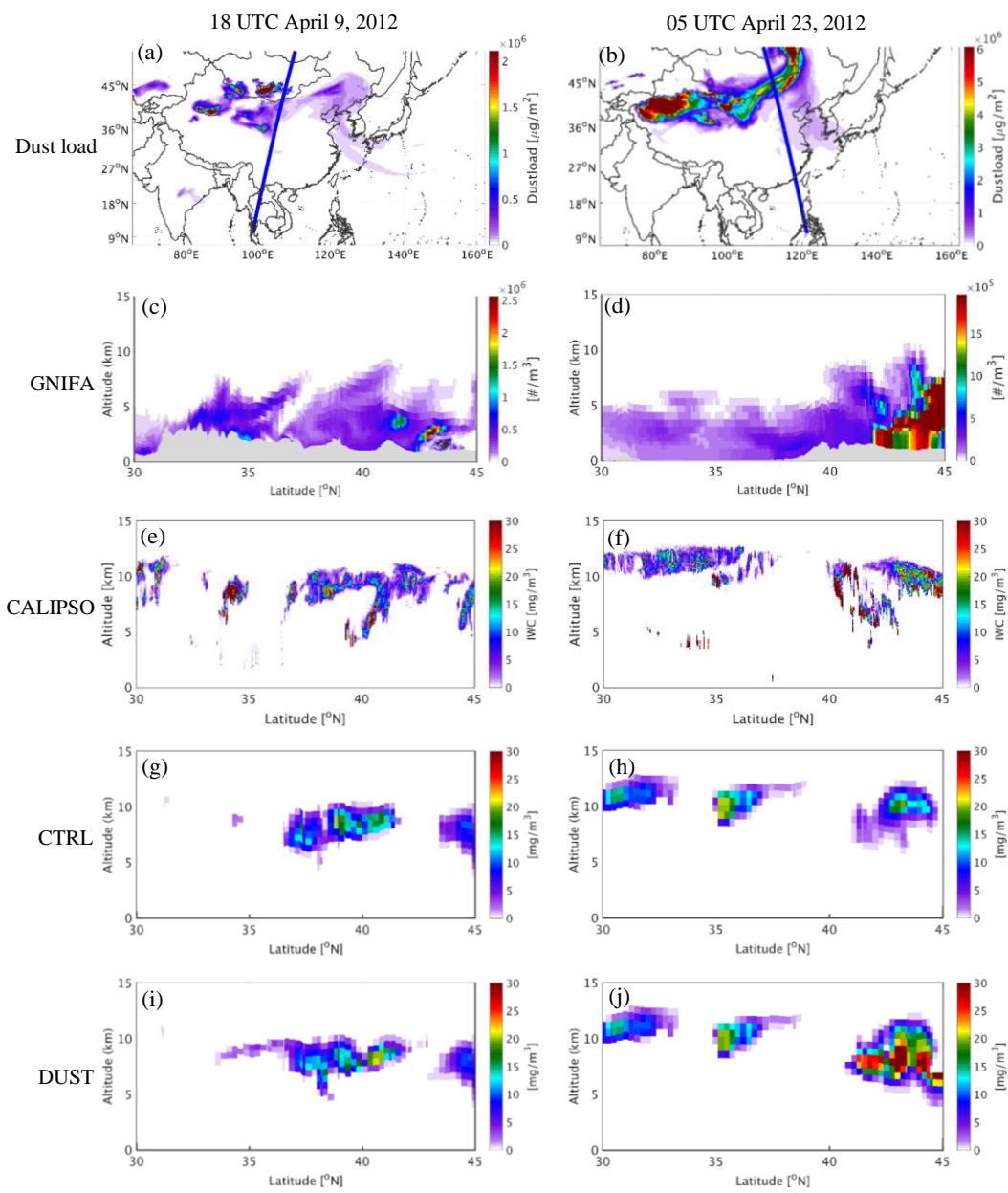


**Figure 9:** As Figure 8 but for the cases on April 9 (left panel) and April 23, (right panel) of 2012.

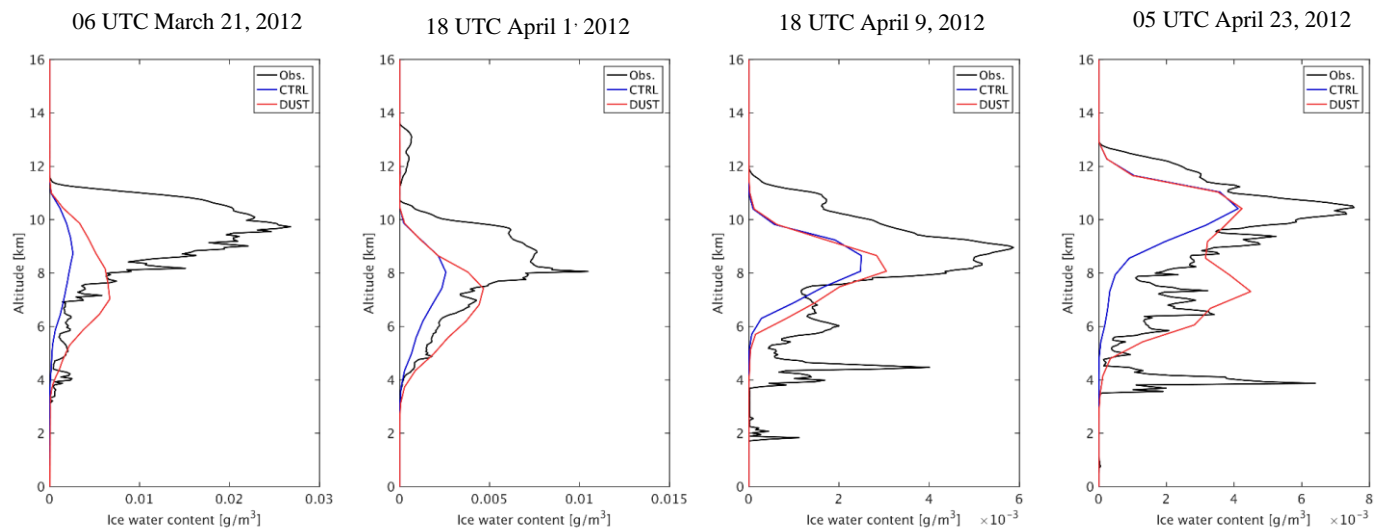


**Figure 10:** Vertical profiles for the mean observed IWC from CALIPSO, and the simulated IWC from CTRL and DUST for dust events on March 21, April 1, April 9, and April 23, 2012.

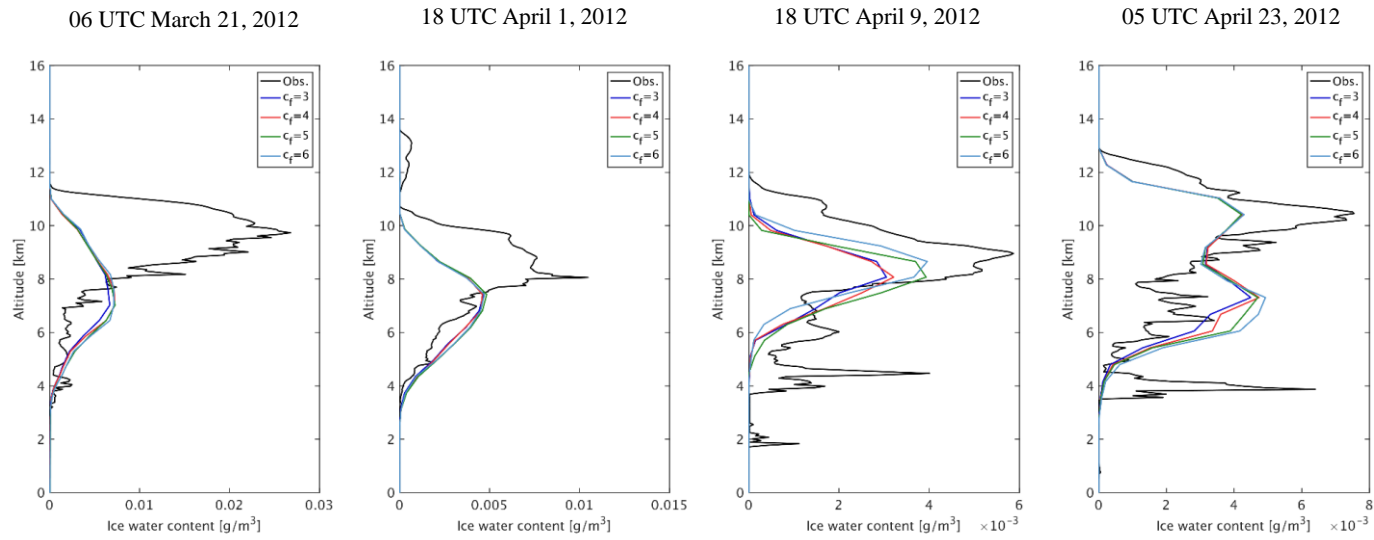


**Figure 11:** Vertical profiles for the mean observed IWC from CALIPSO, and the simulated IWC with various  $c_f$  for the dust events on March 21, April 1, April 9, and April 23, 2012.

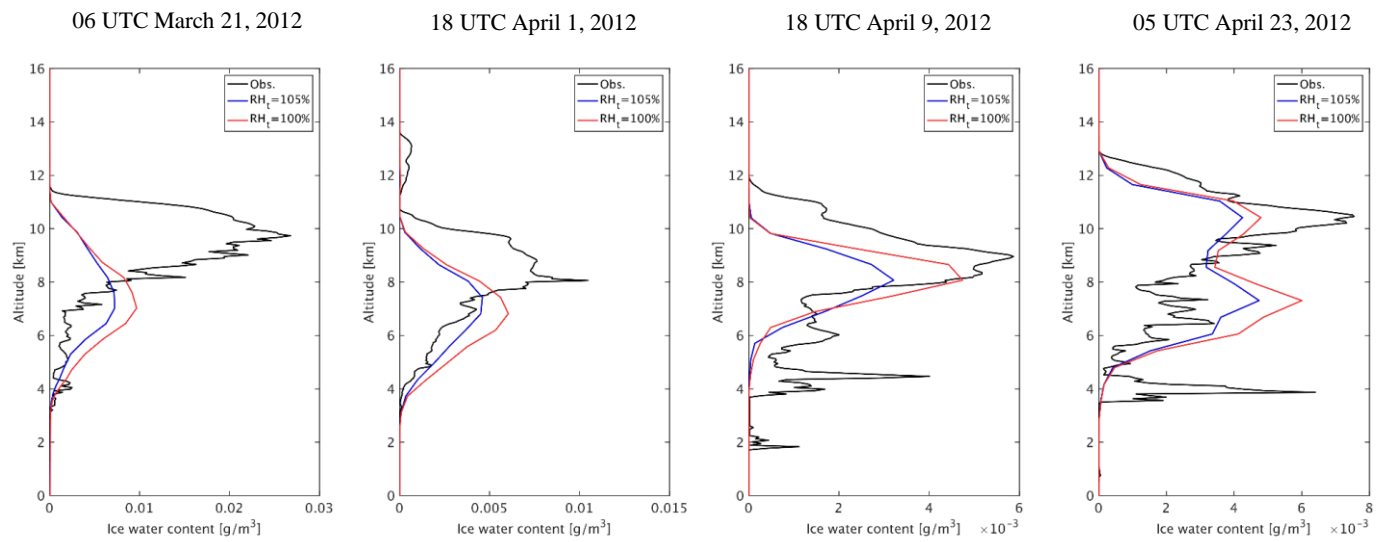


**Figure 12:** Vertical profiles for the mean observational IWC from CALIPSO, and the simulated IWC with threshold RH values of 105% and 100% for the dust events on March 21, April 1, April 9, and April 23, 2012.